

# Mastering lanthanide energy states for next-gen photonic innovation

Yuyang Gu<sup>1</sup>, Chang Gu<sup>1</sup>, Yuxiang Zhang<sup>1</sup>, Zhen Mu<sup>1</sup> & Xiaogang Liu<sup>1,2\*</sup>

<sup>1</sup>Department of Chemistry, National University of Singapore, Singapore 117543, Singapore;

<sup>2</sup>Institute of Materials Research and Engineering, Agency for Science, Technology and Research, Singapore 138634, Singapore

Received March 24, 2023; accepted April 26, 2023; published online August 14, 2023

Lanthanide-based photonic materials have been extensively explored for use in laser crystals, lighting, fiber-optic communications, bioimaging, diagnostics, and many other fields. In recent years, they have enabled numerous breakthroughs in areas such as single-particle spectroscopy, super-resolution imaging, micro-lasing, lifetime multiplexing, and detection. Here, we summarize recent advances in lanthanide photonic materials from an energy state perspective, focusing on the interplay between energy state manipulation and advanced photonic applications. We then discuss the challenges and prospects for controlling energy states at the single-particle level. We wish to highlight the importance of quantifying and understanding the energy states of lanthanides for future innovations.

**lanthanide, nanomaterials, super-resolution, lifetime, lasing**

**Citation:** Gu Y, Gu C, Zhang Y, Mu Z, Liu X. Mastering lanthanide energy states for next-gen photonic innovation. *Sci China Chem*, 2023, 66, <https://doi.org/10.1007/s11426-023-1609-y>

## 1 Introduction

Lanthanide spectroscopy has a long history and has played a key role in the investigation of luminescent materials. In 1908, the sharp absorption peaks of lanthanide (III) ions were discovered by Becquerel *et al.* [1]. The red phosphor YVO<sub>4</sub>:Eu was discovered in the 1960s [2]. Since then, lanthanide-doped phosphors have been widely used in color televisions. Also in the 1960s [3,4], researchers discovered that Yb<sup>3+</sup> can be used as a sensitizer, while Er<sup>3+</sup>, Ho<sup>3+</sup>, and Tm<sup>3+</sup> are used as activators for upconversion [5–8] and that Pr<sup>3+</sup> can undergo quantum cutting [9,10]. Since then, research on upconversion and related laser materials has emerged. In addition, lanthanide phosphors with afterglows have made significant progress since the 1990s [11]. In the 2000s, the wet chemical method for fabricating nanomaterials [12–14] was applied to lanthanide-doped materials [15–

19]. Precise tuning of upconversion has given a major boost to the field [20–23], leading to a boom of applications in luminescence bioimaging, temperature sensing, multicolor multiplexing, spectral conversion for solar cells, three-dimensional (3D) displays, anti-counterfeiting, and preclinical drug delivery and therapy [24–36].

Over the past decade, lanthanide photonic materials have been found to exhibit peculiar advantages in super-resolution microscopy, single-molecule tracking, luminescence nanothermometry, lifetime multiplexing and *in vivo* sensing, thanks to the advances in materials and technology. With the deepening understanding of the multitude of energy levels and interactions, a major transformation is gradually taking place in this field of research. By understanding energy states, it has been possible to achieve “rational design and development” of materials, as opposed to relying on random “treasure hunts” or simple combinations of material functions. Such applications exploit materials in areas that cannot be covered by conventional techniques. This requires the

\*Corresponding author (email: [chmlx@nus.edu.sg](mailto:chmlx@nus.edu.sg))

adaptation and invention of application tools specifically tailored to the material's performance.

After over 20 years of vigorous development in the field of lanthanide photonics, there are still some obstacles in the field. Therefore, a review and analysis of currently available tools seems necessary. This includes a summary of current available theoretical methods and, more importantly, how these tools and insights can sustainably aid in the development and discovery of next generation applications.

In this review, we focus on summarizing some widely used theories for understanding energy states and dynamics, especially in custom-designed nanomaterial systems. We then present some general tools that can accelerate materials advancement. Particular issues from the perspective of energy state manipulation are discussed in detail. We conclude this review by addressing bottlenecks and future directions of work.

## 2 Theoretical background and numerical tools for analyzing lanthanide energy states

### 2.1 f-f energy levels, J-O theory, and luminescence lifetime

Unique f-f transitions and d-f transitions are key to lanthanide emission. In the solid state, lanthanide ions often have a positive trivalent state. The number of  $2^{S+1}L_J$  states can be calculated using optical spectroscopy and quantum mechanical theories. For example, more than one hundred  $4f^N$  states can be calculated for trivalent Nd, Sm, Eu, Gd, Tb, Dy ions. For detailed energy levels, Dieke and Crosswhite [37] had measured a complete energy level diagram (below  $40,000\text{ cm}^{-1}$ ) in  $\text{LaCl}_3$  crystals.

The ample  $4f^N$  energy levels lead to a large number of transitions. These transitions of lanthanide ions (III) are well-described by the J-O theory, developed independently by Judd [38] and Ofelt [39] in 1962. This method has been widely used for the estimation of transition probability, radiation lifetime, emission cross section and other parameters [40,41]. The method can be described briefly as follows: First, measure the material's absorption spectrum and average polarized absorption if needed. The absorption cross section  $\sigma_a$  is given by

$$\sigma_a = \frac{1}{Nl} \ln \frac{I_0}{I} \quad (1)$$

where  $N$  is the number of ions per volume;  $l$  is the measured length of the sample;  $I_0$  and  $I$  are the intensities before and after material absorption. A parameter called line-strength, which is related to the integrated absorption cross section, can be calculated accordingly. With the least square method, the oscillator strength parameter  $\Omega_\lambda$  ( $\lambda = 2, 4, 6$ ) can be fitted in combination with the J-O expression and the

linestrength value.

The above calculation only considers electric dipole transition, but there are other transition contributions. It is usually assumed that only the relatively larger magnetic dipole (md) transition is additionally considered. Its value can be obtained separately and can refer to the calculated results [42].

A detailed description of J-O theory can be found in calculation examples in Refs. [41,43–47].

Notably, various developments and extensions of J-O theory, such as J-Mixing, Electron Correlation, Dynamic Coupling, Wybourne-Downer Mechanism, and Relativistic Contributions, have been proposed to address its limitations in specific situations [41,48].

The set of  $\Omega_\lambda$  parameter can be used to calculate the spontaneous transition probability  $A$ , radiative lifetime, and emission cross section.

The radiative lifetime is given by

$$\frac{1}{\tau_{\text{rad}}} = A \quad (2)$$

This is the lifetime in an ideal situation where there are no other factors such as non-radiative relaxations.

Alternatively, radiative lifetime can be calculated from emission cross section, which can be derived from the absorption cross section described above [49,50].

When nonradiative transitions are involved, the experimental lifetime decreases. The relative quantum yield can be given as the ratio between the experimental lifetime and the radiative lifetime. By comparing the actual lifetime with the radiative lifetime, we can obtain the relative quantum yield:

$$\eta = \frac{\tau_{\text{exp}}}{\tau_{\text{rad}}} \quad (3)$$

This method is mainly used to evaluate the quantum yield of laser crystals with singly doped ions (*e.g.*,  $\text{Nd}^{3+}$ ,  $\text{Tm}^{3+}$ , or  $\text{Yb}^{3+}$ ) [51–53]. It can also be applied to lanthanide complexes that have a single emission center [54,55].

In real crystals,  $4f$  energy levels split into several sublevels (called Stark levels) due to the local crystal field, which complicates spectrum analysis. A typical method for identifying those Stark levels is to measure and compare the absorption and emission spectra at an extremely low temperature (77 K or below). Because of the low temperature, the vibration energy of the crystal structures (known as “phonons”) can be minimized, making the energy band sharp and easy to identify [56]. For broadened room-temperature spectra, a similar estimation can be performed using the Lorentz fitting function. This kind of method is important in laser photonics because the Stark energy levels can act as laser energy levels for four-level systems and three-level systems [57,58].

For an isolated single ion, the luminescence lifetime should obey first-order kinetics. That is, the decay rate  $k$  does

not depend on time:

$$-\frac{dn(t)}{dt} = kn(t) \quad (4)$$

where  $n(t)$  is the time-dependent population of a certain excited state,

$$n(t) = n_0 e^{-kt} \quad (5)$$

where  $n_0$  is the population of the excited state at time 0.

To define the lifetime =  $1/k$ , the above equation can also be described as

$$n(t) = n_0 e^{-\frac{t}{\tau}} \quad (6)$$

The time-independent lifetime is the essence of all lifetime-based detections. For systems and conditions that do not follow this rule, the lifetime would depend on time and other conditions, including the excitation power density. This means that the lifetime will change if excitation conditions are not exactly the same. Such an uncertainty makes it difficult to reproduce results in different laboratories, especially when dealing with samples under biological conditions and in deep tissues [59].

## 2.2 Energy migration, energy transfer and rate equation

The J-O theory successfully describes the intensity and lifetime of lanthanide emission. However, it is applicable only to a single ion. In a complex doped material, energy migration between the same energy levels (of the same ion type) and energy transfer between different ions are sometimes dominant.

To explain this in more detail, there are several possibilities of energy transfer. If the emission spectrum of the donor matches the absorption spectrum of the acceptor, non-radiative resonance energy transfer can occur between the donor and acceptor. If the energy levels do not match, non-radiative phonon-assisted energy transfer can still be observed.

Before we look more closely at the differences in energy transfer, we need to establish a set of equations that can describe these processes kinetically. By solving a series of rigid partial differential equations, the trend of population change of each energy level can be obtained. This information can guide the design of material structures, doping ratios, and energy migration paths.

From the perspective of a kinetic model, the energy transfer rate can be described by a coefficient (usually denoted as  $W$ ) and multiplied by the population of the energy level (excited energy level of the donor and ground energy level of the acceptor) in the rate equation. For a typical energy transfer process, for example, the rate equation can be given as follows:

$$\begin{aligned} \frac{dN_0}{dt} &= -GN_0 + k_1N_1 + WN_1N_3 \\ \frac{dN_1}{dt} &= GN_0 - k_1N_1 - WN_1N_3 \\ \frac{dN_2}{dt} &= WN_1N_3 - k_2N_2 \\ \frac{dN_3}{dt} &= -WN_1N_3 + k_2N_2 \\ N_A &= N_0 + N_1 \\ N_B &= N_2 + N_3 \end{aligned} \quad (7)$$

where  $N_0$  and  $N_1$  are the population concentrations of donor A in the ground-state and excited-state,  $N_2$  and  $N_3$  are the population concentrations of acceptor B in the ground-state and excited-state, and  $N_A$  and  $N_B$  are the concentrations of donor A and acceptor B, respectively;  $W$  is the energy transfer rate from A to B;  $k_1$  and  $k_2$  are the decay rates (including non-radiative decay) of A and B, respectively;  $G$  is the excitation rate of donor A.

The energy transfer rate can be estimated by comparing the lifetime of the donor with and without the acceptor. The details are explained below [60,61].

For a given donor-acceptor system, the lifetime  $\tau$  of the donor can be described by

$$\tau = \frac{1}{k + k_{nr}} \quad (8)$$

which includes  $k$  (radiative decay rate) and  $k_{nr}$  (nonradiative decay rate).

It can also be given as

$$\frac{1}{\tau_{\text{donor}}} = k + k_{nr} \quad (9)$$

When an energy acceptor is introduced into the system, the energy transfer from the donor to acceptor occurs, and the lifetime of the donor would change:

$$\frac{1}{\tau_{\text{donor(acceptor)}}} = k + k_{nr} + W_{\text{donor-acceptor}} \quad (10)$$

where  $\tau_{\text{donor(acceptor)}}$  is the lifetime of the donor in the presence of the acceptor, and the energy transfer rate  $W_{\text{donor-acceptor}}$  can be given as

$$W_{\text{donor-acceptor}} = \frac{1}{\tau_{\text{donor(acceptor)}}} - \frac{1}{\tau_{\text{donor}}} \quad (11)$$

The energy transfer efficiency from the donor to the acceptor ( $\eta_{\text{donor-acceptor}}$ ) can be calculated using the following equation:

$$\eta_{\text{donor-acceptor}} = 1 - \frac{\tau_{\text{donor(acceptor)}}}{\tau_{\text{donor}}} \quad (12)$$

The decay rate can also be obtained by measuring the lifetime. With the known energy transfer rate and decay rate, the kinetics of a typical energy transfer system can be simulated numerically by solving these partial differential equations. With the simulation tools (e.g., MATLAB or Python, which have built-in algorithms), rate equations are widely used in laser dynamics, super-resolution, energy migration, and transfer studies.

### 2.2.1 Estimating the energy transfer rate from theory

From a microscopic perspective, energy transfer occurs when the energy level of a donor in the excited-state matches that of an acceptor. In his pioneering study, Dexter [62] investigated the dipole-dipole and dipole-quadrupole interactions between energy donors and acceptors, enabling the calculation of energy transfer rates using experimentally measured spectroscopic parameters.

However, the situation for 4f transitions in lanthanide ions is slightly different. In 1973, Kushida [63] developed expressions for the energy transfer rate based on the results of the Judd-Ofelt theory. These expressions account for the combined effects of dipole-dipole (d-d), dipole-quadrupole (d-q), and quadrupole-quadrupole (q-q) interactions.

In detail, the rate of energy transfer derived from dipole-dipole interactions is inversely proportional to the sixth power of the distance ( $R^6$ ) between the energy donor and acceptor. Likewise, the energy transfer rates for dipole-quadrupole and quadrupole-quadrupole interactions are inversely proportional to the eighth ( $R^8$ ) and tenth ( $R^{10}$ ) powers of the distance, respectively.

By considering the shielding effects of 4f electrons and conducting a comprehensive analysis, Malta et al. [64,65] have shown that the quadrupole-quadrupole mechanism dominates the energy transfer rate, as opposed to the previously assumed dipole-dipole mechanism. Detailed analysis can be found in references.

### 2.2.2 Phonon-assisted energy transfer

The above-mentioned theories describe conditions under which spectral overlap occurs between donor emission and acceptor absorption. However, in some systems without overlap, energy transfer does occur. This can be explained by phonon-assisted energy transfer [66]. During energy transfer, one or more “phonons”, or quantized energy of crystal vibration, are absorbed or emitted, resulting in energy equilibrium.

The probability of phonon-assisted energy transfer from donor to the acceptor  $W_{\text{donor} \rightarrow \text{acceptor}}(T)$  can be given as [67]

$$\begin{aligned} W_{\text{donor} \rightarrow \text{acceptor}}(T) &= A \times [1 + n_{\text{ph}}(T)]^n \\ &\times \int \frac{\sigma_{\text{em}}^{\text{donor}}(T, E - nE_{\text{ph}}) \sigma_{\text{abs}}^{\text{acceptor}}(T, E)}{E^2} dE \\ &= A \times [1 + n_{\text{ph}}(T)]^n I_{\text{ov}}(T, n, E_{\text{ph}}) \end{aligned} \quad (13)$$

where  $A$  is a temperature-independent constant and  $I_{\text{ov}}(T, n, E_{\text{ph}})$  is the phonon-assisted spectral overlap integral between donor emission and acceptor absorption (assuming that this overlap does not change at different temperatures).  $\sigma_{\text{em}}^{\text{donor}}$  is the emission cross section of the donor, and  $\sigma_{\text{abs}}^{\text{acceptor}}$  is the absorption cross section of the acceptor.

$n_{\text{ph}}(T)$  is the phonon density associated with temperature.

$$n_{\text{ph}}(T) = \left( e^{\frac{E_{\text{ph}}}{kT}} - 1 \right)^{-1} \quad (14)$$

$E_{\text{ph}}$  is the phonon energy and meets the requirement of  $\Delta E = nE_{\text{ph}}$  (15)

where  $n$  is the number of phonons involved in the process and  $\Delta E$  is the energy mismatch in donor and acceptor.

The temperature-dependent energy transfer rate  $W_{\text{donor} \rightarrow \text{acceptor}}$  can be fitted by the equation of phonon-assisted energy transfer probability ( $A \times [1 + n_{\text{ph}}(T)]^n$ ). The number of phonons involved in the process can be estimated based on the best fit of the energy transfer rate.

From these interpretations, we can learn that a good way to identify phonon-assisted energy transfer is to use temperature-dependent measurements of the luminescence spectrum or lifetime.

### 2.2.3 Simulation of energy migration using the Monte Carlo algorithm

Recently, energy transfer within the same kind of lanthanide ions (usually referred to as energy migration) has been of great interest. Controlling the migration length of lanthanide ions (usually  $\text{Yb}^{3+}$  ions) is an efficient way to manipulate the temporal luminescence properties of lanthanide materials. A more quantitative view can be obtained using Monte Carlo simulation methods. Considering lanthanide ions as “spheres” and the energy transfer/migration between them as “collision of spheres”, this method can provide semi-quantitative results for the energy migration and transfer based on a microscopic random picture. Because of the microscopic view of the simulation system, the localized energy transfer in layered structures can be precisely simulated. This is not possible with other simulation techniques.

In a representative work, Monte Carlo simulation is used to explain and predict the energy migration dynamics in a core-shell-shell structure [68]. Based on this new understanding, the upconversion rise and decay time can be finely controlled [69]. Similar methods can also be applied to quantify internal hydroxyl impurities in  $\text{NaYF}_4$  crystals [70] and help reveal the energy dissipation routes for dye-sensitized upconversion [71].

## 2.3 Dynamics of lanthanide luminescence in an enhanced electromagnetic field

When lanthanide materials are placed in a cavity, the quantum electrodynamic (QED) effect of the cavity can modify the spontaneous emission rate of the material. In 1946, Purcell [72] proposed what later became known as the

“Purcell effect” to quantitatively describe this phenomenon. The enhancement factor between the cavity-coupled emission rate and the spontaneous emission rate  $\eta$  can be described as

$$F_p \propto \frac{Q}{V_m} \left( \frac{\lambda}{n} \right)^3 \quad (16)$$

where  $Q$  is the quality factor of the cavity,  $n$  is the refractive index of the cavity,  $\lambda$  is the lasing wavelength, and  $V_m$  is the volume of the cavity mode. A larger quality factor and a smaller volume of the cavity increase the enhancement factor. In other words, the optical cavity should store light in the smallest possible volume and for the longest possible time. This can be demonstrated in photonic crystals and metal nanostructures [73].

The accelerated emission rate in the cavity offers opportunities to explore new luminescence processes. An inspiring example [74] is the observation of  $\text{Nd}^{3+}$  emission at 800 nm in the optical cavity. Normally, this emission band is heavily quenched by the cross-relaxation of  $\text{Nd}^{3+}$  and cannot be observed. Because of the QED effect, the spontaneous emission rate becomes larger than the competing cross-relaxation rate and thus becomes detectable. However, there is still very little work on manipulating energy levels in the optical cavity, or on manipulating energy transfer rates. A microscopic cavity, along with new emission dynamics, would certainly open the doors for photonic integrations, such as optical communications, information storage, and miniature laser sources.

For a more comprehensive view, the above rate equation model can also be used to simulate the energy flux in the laser cavity. For example, in a typical four-level system (the four energy levels are denoted as  $n_0$ ,  $n_1$ ,  $n_2$ , and  $n_3$ , energy from the lowest to the highest), a set of rate equations can also be established in addition to the laser operation:

$$\begin{aligned} \frac{dn_3}{dt} &= n_0 W_{03} - n_3 (S_{32} + A_{30}) \\ \frac{dn_2}{dt} &= n_1 W_{12} - n_2 W_{21} - n_2 (A_{21} + S_{21}) + n_3 S_{32} \\ \frac{dn_0}{dt} &= n_1 S_{10} - n_0 W_{03} + n_3 A_{30} \\ n_0 + n_1 + n_2 + n_3 &= n \\ \frac{dN_l}{dt} &= -n_1 W_{12} + n_2 W_{21} - \frac{N_l}{\tau_{\text{Rl}}} \end{aligned} \quad (17)$$

In the above equations,  $n_3 W_{30}$  is omitted.  $N_l$  is the photon number density (per unit volume) in the  $l$ th mode, and this mode has a photon lifetime of  $\tau_{\text{Rl}}$ .  $A_{\text{ab}}$  and  $S_{\text{ab}}$  are the spontaneous radiative decay rate and the nonradiative decay rate from energy level  $n_a$  to energy level  $n_b$ .  $W_{12}$  and  $W_{21}$  are the stimulated absorption rate and stimulated emission rate, respectively. A detailed analysis of cavity dynamics can be found in classic laser textbooks [75,76].

Simulation of laser kinetics can be quite helpful in the

design of laser resonators and materials. For example, when a saturable absorber is inserted into the laser cavity, laser operation in  $Q$ -switched mode can be simulated [77,78]. Detailed analysis of cavity effect can be found in examples in Section 4.3.

## 2.4 X-ray persistent luminescence

X-rays are also referred as Röntgen radiation after their first discovery by a German scientist W.C. Röntgen in 1895 [79]. His discovery paved the way for developing luminescent materials capable of effectively absorbing X-rays and converting them into longer wavelength light [79]. Unlike photoinduced luminescence, X-ray-activated luminescence features not only ultrahigh excitation energy but also a totally different mechanism [80]. During X-ray irradiation, electrons in the inner shell of host atoms are excited and scattered in the lattice by the photoelectric effect and Compton scattering effect. As a result of electron-electron scattering and the Auger process, massive free electrons and holes with energies comparable to the band gap are generated. When an enormous number of free electrons and holes recombine, energy is transferred to the luminescence center in the crystal lattice, whereupon light emission occurs. Apart from light emission upon X-ray radiation, in some cases energy can be stored in traps and persistently released under thermal or light excitation after the excitation is terminated. This optical phenomenon is called afterglow. Two things happen during excitation by X-rays. First, the electrons jump from the valence band to the conduction band, leaving a large number of holes in the valence band. Second, ions in the host materials (e.g., F and O) are likely to be ejected from their original sites, creating vacancies and interstitial ions that can trap electrons and holes in conduction and valence bands. After the X-ray source is ceased, electrons and holes gain enough energy to escape from the traps and return to the conduction or valence band under stimulation by heat or light. The luminescent atom attracts an electron-hole pair or attracts an electron and a hole due to the Coulomb force. Subsequently, the luminescent atom gains energy from the electron-hole pair recombination and jumps to the excited state, leading to persistent luminescence.

## 3 Instrumentation

As there is a growing need for original photonic applications, the necessary optical tool has become increasingly important. Novel optical tools and algorithms have played a key role in revealing new optical phenomena under challenging and unconventional conditions. Therefore, we hope to develop a common understanding of optical design among researchers studying lanthanides by summarizing some of

the most widely used optical components and some state-of-the-art optical systems based on recent work.

### 3.1 Excitation sources and detectors for lanthanide emission

Lanthanide ions are known for their narrow absorption band and small absorption cross section. Most excitation sources must be coherent to produce strong luminescence. Single-mode and multimode laser sources differ in power (the former is less than 500 mW, and the latter can produce up to hundreds of watts of optical power) and beam quality, but do not differ significantly in a common wide-field microscope. Single-mode lasers are required for some demanding applications, such as manipulating the state of polarization or focusing the laser to a diffraction-limited spot. Multimode lasers also introduce laser speckles that can cause artifacts on the image plane. For tunable laser sources, optical parametric oscillators (OPO) produce tunable wavelengths ranging from ultraviolet to infrared, with output power varying with the pump source. Typically, using Nd YAG or diodes as the pump source, they deliver  $\mu\text{J}$  to mJ nanosecond pulses at low repetition rates (usually below 100 Hz). They are widely used in spectroscopy to excite lanthanide materials for lifetime studies. Once the laser beam is focused to a microspot, materials are easily saturated due to the high power density. This makes them useful for measurements at high power and under extreme conditions. For picosecond laser diodes and tunable femtosecond lasers, the repetition rate is usually high (several hundred kHz to MHz) with reduced single short power (usually below  $\mu\text{J}$ ). As lanthanides decay slowly over at least several  $\mu\text{s}$ , lasers continuously excite them before they fully decay. As a result, these lasers are not suitable for kinetic or lifetime studies of lanthanides, but they are useful as high-quality excitation sources.

On the detector side, a fluorescence spectrometer is usually equipped with a photomultiplier tube. These vacuum tubes can multiply electrons and provide over  $10^6$  gain in the ultraviolet-visible (UV-Vis) range. They are suitable for single point detection. Alternatively, a single-photon avalanche diode is an avalanche photodiode that uses reverse bias, which provides single-photon detection and extends the wavelength to over 1,000 nm. Both detectors have good sensitivity and temporal resolution and are widely used in spectroscopy and scanning-based microscopy.

As for array detectors, both charge-coupled device (CCD) detectors and scientific complementary metal-oxide-semiconductor (sCMOS) detectors are well suited for luminescence imaging. For low-light applications, the electron multiplying charge-coupled device (EMCCD) is the most widely used camera for single-particle imaging and tracking. On the other hand, intensified cameras can also reach the range of single-photon detection, but with sacrifices in

quantum efficiency (QE). Additionally, intensified cameras are equipped with image intensifiers that can act as nanosecond electronic shutters, allowing direct time-resolved imaging. A similar camera that provides optical gating is the two-tap camera, which is used in industry as time-of-flight sensors. Recently, single-photon avalanche diode (SPAD) arrays with microlenses have been introduced as SPAD cameras. They offer photon counting capability, making them useful for imaging applications that require a high degree of precision.

For the near-infrared (NIR) wavelength range (900–1,700 nm), the choice of detectors is quite limited. There are single photon detectors, superconducting nanowire detectors and InGaAs cameras that have been used in scientific studies. These are rather expensive and usually require heavy cooling to reduce noise. With advances in semiconductor technology, more commercial-grade NIR sensors are expected.

### 3.2 Representative optical systems

Table 1 lists some typical imaging systems that have been used recently in lanthanide photonics. A detailed discussion is given below.

#### 3.2.1 Wide-field macroscope and microscope systems

A wide-field macroscope or microscope is the most commonly used equipment in physical and biological luminescence studies. It is usually equipped with excitation sources, a dichroic mirror and filter set to separate excitation and emission, an objective (or lens set), a tube lens for imaging on the detector, and a detector for signal collection. Depending on the field of view, objectives with different magnifications or lens sets with different focal lengths can be used. A wide-field macroscope can be used for visualizing chips, devices, and biological samples such as small animal parts. A wide-field microscope is mostly useful for visualizing cells, bacteria, and microscopic materials. With customized excitation and detection options, a wide-field microscope can detect multiple signals with maximum efficiency, such as upconverted and downshifted luminescence, second or multiple harmonic generation, Raman signals, and lasing.

A wide-field set up can also produce super-resolution images when used with photoswitchable or fluctuating fluorophores, such as stochastic optical reconstruction microscopy (STORM), photo-activated localization microscopy (PALM) or super-resolution optical fluctuation imaging (SOFI). By adding a spatial light modulator and a corresponding optical path, a structured illumination microscopy (SIM) scheme can improve resolution down to half the diffraction limit. For wide-field time-resolved imaging over a wide range, an optical chopper and a pinhole can be inserted to the optical path and act as an “on-off” shutter in the image plane.

**Table 1** Selected optical setups, key concepts, applications, and advantages for lanthanide photonics research in recent years

System	Key concept	Application in lanthanide fields	Advantage	Ref.
Wide-field luminescence microscope	Wide-field illumination	Single particle imaging and tracking	High efficiency, high frame rate	[81,82]
Wide-field lifetime imaging macro/microscope	Optical chopper, wide-field imaging	Time-gated imaging, lifetime imaging	Time-gated imaging of micro to millisecond lifetime	[59,83–85]
Structured illumination microscope	Spatial light modulation, widefield imaging	Super-resolution microscopy	High efficiency, high frame rate	[86]
Light-sheet structured illumination microscope	Galvo scanner, structured illumination	Noninvasive <i>in vivo</i> imaging	Deep tissue with improved resolution, 3D imaging	[87]
Confocal scanning microscope	Galvo scanner, confocal design	Near infrared imaging in deep tissue; nonlinear super-resolution microscopy	Optical sectioning, high excitation power, high resolution imaging	[88–91]
Confocal scanning lifetime microscope	Pulsed excitation and real time collection	Lifetime-based multiplexing	High lifetime resolution	[92,93]
Two-beam confocal microscope	Donut beam formed by vortex waveplate, piezo stage scanning	Stimulated emission depletion super-resolution microscopy	High excitation power, best resolution	[94,95]

### 3.2.2 Scanning-based confocal systems

A confocal system usually uses a focused, diffraction-limited beam to scan samples. Scanning can be achieved either by moving the stage in steps, or by using two steering mirrors in  $x$  and  $y$  directions (known as galvanometers). The beam scanning method offers good adjustability of beam shape and intensity. For example, a polarized single-mode laser beam can be modulated by a vortex waveplate into a Laguerre-Gaussian beam with a “donut” intensity distribution. This is used as a depletion beam in stimulated emission depletion (STED) super-resolution microscopy. Although the excitation beam is focused to enhance luminescence, the point-by-point scanning scheme is usually slower and less efficient than a wide-field system.

The construction of a confocal system is usually more complicated than that of a wide-field system. There are a number of protocols that can help in building a variety of confocal systems [96–100] and confocal-based super-resolution systems [101–103]. In addition, combining some cheap modular components is a good solution [104].

## 4 Controlling energy states and interactions of lanthanides for various photonic applications

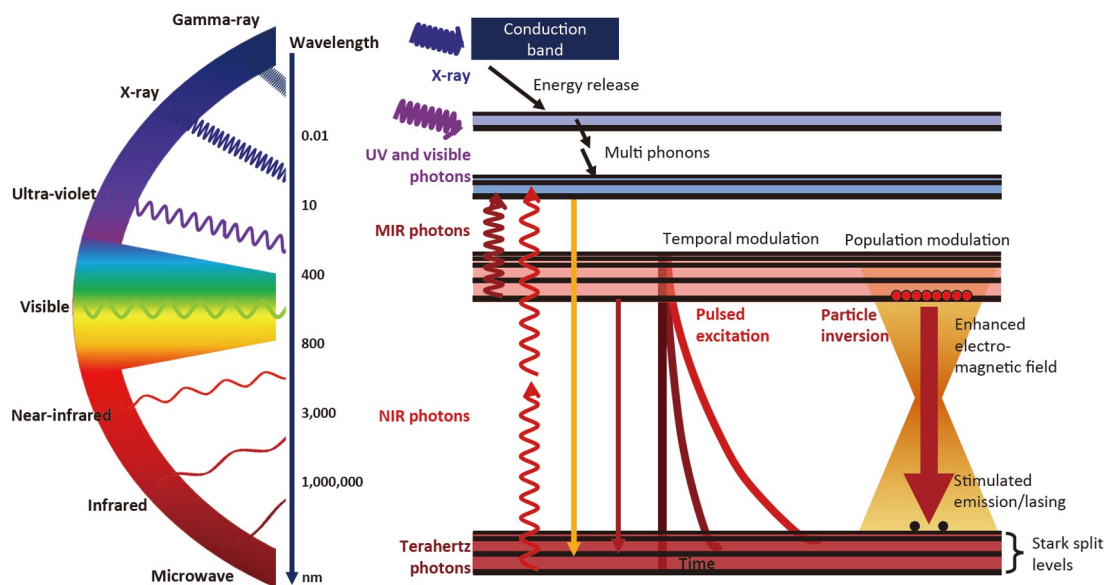
In Scheme 1 and Table 2, we provide an overview of recent advancements in manipulating the energy states of lanthanide materials. We summarize primary methodologies using keywords based on energy level states and excitation or detection techniques. Additionally, we highlight the respective application fields and key advances for each method.

### 4.1 Manipulating energy states for super-resolution microscopy

Direct observation of subcellular structures and life processes is important for modern biological research. However, due to the diffraction phenomenon, classical linear optical microscopy generally has the problem of limited resolution. In 1873, Abbe *et al.* [116] proposed the optical diffraction limit  $\lambda / (2 \times NA)$ , where  $\lambda$  is the wavelength and  $NA$  is the numerical aperture. To overcome this challenge, super-resolution microscopy has witnessed rapid development in recent years. Due to the excellent upconversion luminescence properties detectable down to single nanoparticles, they have been widely used in developing super-resolution microscopes, including STED microscopy [94,95,108,117–123], FED microscopy [109,111,124–126], and SIM [86]. Traditionally, super-resolution imaging techniques have been primarily concerned with improving optical systems. In contrast, the breakthrough of lanthanide-based super-resolution techniques focused mainly on the material side. More specifically, the key lies in tuning the energy state of lanthanides. Here we will discuss how super-resolution can be achieved by manipulating the energy states of lanthanide ions.

#### 4.1.1 Super-resolution based on population inversion

As one of the key factors in laser formation, population inversion has been extensively studied for many years. Among various forms of population inversion, the multi-step long-lived energy levels of lanthanide ions facilitate the transition of electrons from the ground state to the high-energy excited state after continuous pumping. It is possible to accumulate and invert populations using lanthanide-doped UCNPs at these fixed intermediate energy levels, which has great



**Scheme 1** Manipulation of excitation energy and energy states for advanced photonic applications. Left, an electromagnetic spectrum showing the possible wavelength range that can interact with lanthanide energy levels. Right, a simplified energy diagram of lanthanide ions with multiple photophysical properties, including multiphonon relaxation and photon absorption in the range from X-rays to terahertz. An illustration of temporal and external electromagnetic field modulation is also included. The illustrations of energy levels and wavelengths are not to scale (color online).

potential for STED research.

Recently, Jin and coworkers [95] synthesized UCNPs with highly doped thulium ions for STED studies. At 980 nm excitation, population inversion is observed at the intermediate  $^3\text{H}_4$  metastable level. Due to the photon-avalanche effect caused by the high  $\text{Tm}^{3+}$  doping, the amplified stimulated emission (ASE) to discharge the  $^3\text{H}_4$  level can be triggered with an 808 nm laser, which is important for increasing the STED efficiency. Based on this method, an optical resolution of 28 nm was achieved in imaging a 13 nm  $\text{NaYF}_4:\text{Yb}/\text{Tm}$  nanoparticle. Almost at the same time, Zhan and coworkers [108] also reported the use of interionic cross relaxation in UCNPs for STED. Based on this principle, they have developed an efficient optical depletion method caused by the strong cross-relaxation between low-lying states of the emitters ( $\text{Tm}^{3+}: ^3\text{H}_4 + ^3\text{H}_6 \rightarrow ^3\text{F}_4 + ^3\text{F}_4$ ). Benefiting from this efficient optical depletion mechanism and low laser intensity requirement, they have achieved two-color super-resolution imaging with a single excitation/exhaustion laser beam pair and immunolabeling of fine subcellular structures with the best image resolution of 82 nm. In addition to depletion of the population-inversed intermediate level, another method can be used to directly deplete the population-inversed level. Our group reported downshifting lanthanide nanoparticles that enable background-suppressed STED imaging in all-NIR spectral regions. Due to the long-lived ( $> 100 \mu\text{s}$ ) metastable states and quasi-four-level configuration, the suppression of luminescence can reach 98.8% at  $19 \text{ kW cm}^{-2}$  saturation intensity. A 70-nm resolution in deep tissue imaging was achieved with this all-NIR method [94].

#### 4.1.2 Super-resolution based on nonlinear effects

Maria Goeppert Mayer first predicted the optical nonlinear effect of two-photon absorption in 1931 [127]. This discovery has since become an essential part of optical research, leading to the development of technologies such as two photon absorption (TPA), second harmonic generation (SHG), and optical parametric amplification (OPA). For super-resolution imaging, nonlinear PSF, photon avalanche and excitation saturation have been used to exploit the nonlinear relationship between fluorescence and excitation light intensity in UCNPs.

For example, Denkova and coworkers [88] reported superlinear excitation-emission (SEE) microscopy in  $\text{NaYF}_4:\text{Yb}/\text{Tm}$  UCNPs. This superlinear characteristic improved the resolution by reducing the FWHM. The best resolution of 206 nm in this system was estimated by measuring the peak-to-peak distance of two single particles. Photon avalanche can also be used for super-resolution, as demonstrated by Schuck and coworkers [89]. They used continuous lasers to pump specially designed  $\text{NaYF}_4:\text{Tm}$  UCNPs and found that the emission scales nonlinearly with the 26<sup>th</sup> power of the pump intensity. This was due to positive optical feedback in each nanocrystal, leading to sub-70 nm spatial resolution using simple confocal microscopy. Shortly thereafter, Zhan and coworkers [90] reported a mechanism of migrating photon avalanche (MPA) in  $\text{NaYF}_4:\text{Yb}/\text{Pr}$  UCNPs. They found that the avalanching  $\text{Yb}^{3+}$  ions can migrate their optical nonlinear response to other emitters in the outer shell layer, boosting the response of  $\text{Tm}^{3+}$  from 26<sup>th</sup>-order in the core to 46<sup>th</sup>-order in the shell. This MPA emitter achieved a

**Table 2** Methods for manipulating the energy states of lanthanide materials used in super-resolution, lifetime microscopy, lasing and other related applications <sup>a)</sup>

Method	Materials	Application	Advances	Ref.
Controlling decay pathway	NaGdF <sub>4</sub> :Yb/Er (18/2%) NaGdF <sub>4</sub> :Yb/Tm (49/1%) NaGdF <sub>4</sub> :Yb (5%)	Luminescence enhancement	Ligand coordination for surface reconstruction	[105]
Enhanced energy transfer	β-NaYF <sub>4</sub> :Yb/Tm(or Ho, Er)	Luminescence enhancement, anticounterfeiting	Thermal enhancement of upconversion	[106]
Excited state absorption	NaYF <sub>4</sub> :Nd@NaYF <sub>4</sub>	High-efficiency MIR sensing and imaging	Broadband MIR detection	[107]
Depletion of population-inversed intermediate level	β-NaYF <sub>4</sub> :Yb/Tm(20/8%) β-NaYF <sub>4</sub> :Yb/Tm(18/10%)	STED imaging of UCNPs and UCNPs labeled cellular cytoskeleton protein desmin	STED with UCNPs with relatively low power depletion	[95,108]
Direct depletion of population-inversed level	NaYF <sub>4</sub> :Nd(1%)	STED imaging of cells stained with nanoparticles and through tissues	NIR with deep tissue; lower power depletion	[94]
Upconversion power dependency	NaYF <sub>4</sub> :Yb/Tm(20/8%)	Super-resolution imaging in neuronal cells	Demonstration of nonlinear-based resolution improvement	[88]
Photon avalanche (high-order power dependency)	NaYF <sub>4</sub> :Tm(8%) NaYF <sub>4</sub> :Yb/Pr(15/0.5%)	Super-resolution imaging of particles and subcellular filament	Discover and optimize high order photon avalanche for super-resolution	[89,90]
Excitation saturation (detection of population-inversed level)	NaYF <sub>4</sub> :Yb/Tm(20/4%) NaYF <sub>4</sub> :Yb/Tm(40/4%)	Super-resolution imaging of particles and in deep tissues SIM imaging of particles and through tissue	Near-infrared emission saturation (NIREs) nanoscopy Nonlinear saturated SIM using UCNPs	[86,109]
Orthogonal excitation and emission	NaGdF <sub>4</sub> :Yb/Er@NaYF <sub>4</sub> @NaYF <sub>4</sub> :Yb/ Tm@NaYbF <sub>4</sub> :Nd@NaYF <sub>4</sub> NaYF <sub>4</sub> :Er@NaYF <sub>4</sub> @NaYF <sub>4</sub> :Yb/Tm <sup>3+</sup>	Fingerprint imaging, lifetime multiplexing Imaging of UCNP ribbons and particles	Excitation orthogonalized upconversion FED nanoscopy	[110,111]
Time-gated imaging	NaYbF <sub>4</sub> @CaF <sub>2</sub>	Multiplexed bio imaging	Highly efficient time-gated detection at the same energy level	[112]
Energy transfer-based lifetime change	NaYF <sub>4</sub> :Yb <sup>3+</sup> /Tm <sup>3+</sup>	Data storage and document security	Lifetime multiplexing Lifetime sensing	[92]
Migration-based lifetime change	NaGdF <sub>4</sub> @NaGdF <sub>4</sub> :Yb/Er @NaYF <sub>4</sub> :Yb@NaNdF <sub>4</sub> :Yb	Multiplexed NIR II imaging of tumour biomarkers	NIR-II lifetime multiplexing	[84]
External cavity-controlled dynamics	NaGdF <sub>4</sub> :Yb <sup>3+</sup> /Er <sup>3+</sup>	Ultrafast upconversion fluorescence	Nanoseconds level and high luminescence intensity	[113]
X-ray-induced persistent luminescence	NaLuF <sub>4</sub> :Tb@NaYF <sub>4</sub> NaYF <sub>4</sub> :3%Er@NaYF <sub>4</sub>	Flat-panel-free, high-resolution, three-dimensional X-ray imaging High-contrast bioimaging in NIR-II window	Lanthanide nanoscintillators Extended emission lifetime in the second near-infrared window	[114,115]

a) FED: fluorescence emission difference; PSF: point spread function; MIR: mid-infrared; Ln, lanthanide; UCNPs: upconversion nanoparticles, MOF: metal-organic framework.

resolution of 62 nm in bioimaging under a continuous low-power laser beam of 852 nm (Figure 1).

Apart from nonlinear PSF and photon avalanche, excitation saturation is an excellent nonlinear optical phenomenon for detecting nonlinear fluorescence signals. Jin and coworkers [109] developed an FED-like nanoscopy for deep tissue imaging and achieved a resolution of sub-50 nm using a doughnut 980 nm beam. This method is based on the near-infrared emission saturation of NaYF<sub>4</sub>:Yb/Tm UCNPs. Based on the same principle, they also demonstrated an

upconversion nonlinear SIM strategy. Using structured illumination with sinusoidal patterns, they found that the nonlinear emission response of an NaYF<sub>4</sub>:Yb/Tm single nanoparticle can generate high spatial frequency components in the Fourier domain, leading to a resolution of 131 nm [86].

The potential to utilize subtle phenomena in lanthanide ions for super-resolution is promising due to their unique and complex energy states. Ongoing exploitation of lanthanide emissions will certainly open doors for future advancements in super-resolution technology.

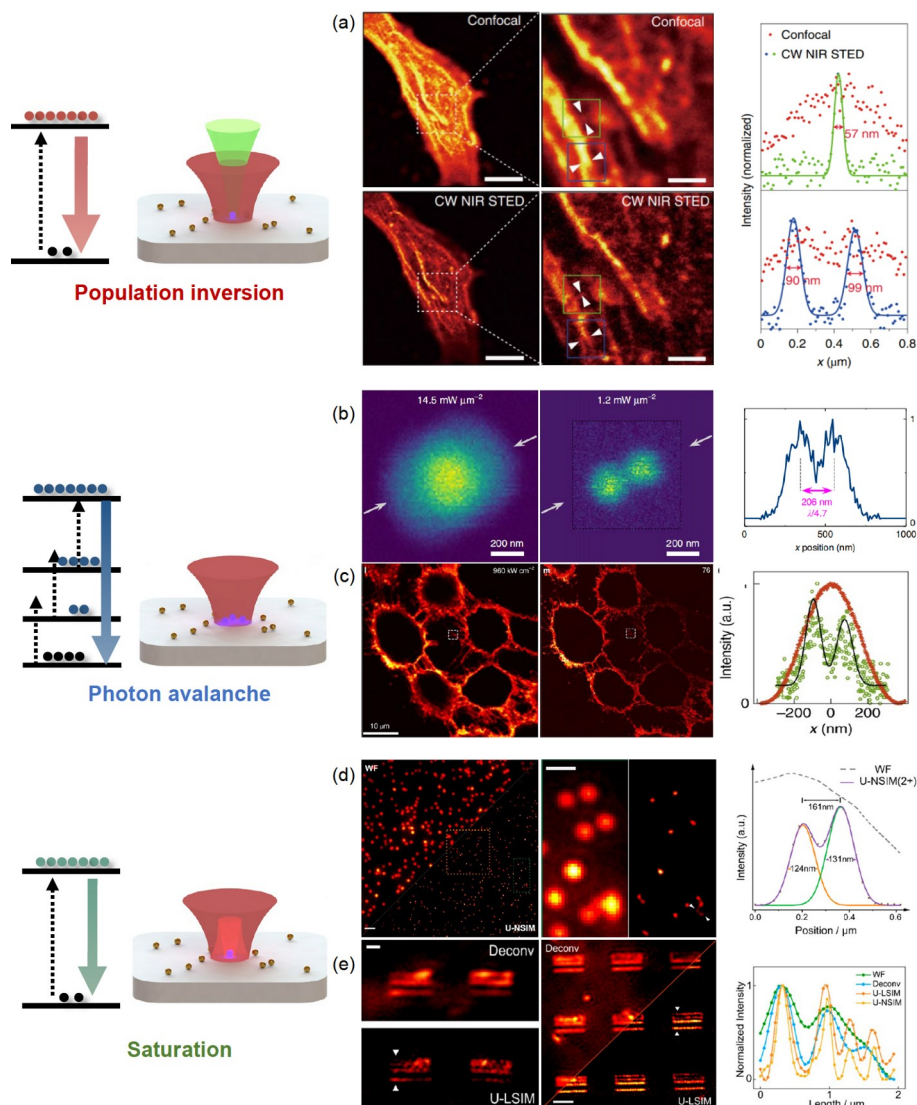


**Figure 1** Manipulation of lanthanide energy states for super-resolution microscopy. (a) Imaging in standard and super-resolution modes of HeLa cells stained with neodymium STED nanoprobes and intensity profile analysis of selected areas. Adapted with permission from Ref. [94], copyright by Springer (2021). (b) Comparative diffraction-limited imaging and superlinear excitation-emission microscopy of two UCNPs separated by 206 nm. Line scans are obtained through a cross-section indicated by gray arrows. Adapted with permission from Ref. [88], copyright by Springer (2019). (c) Super-resolution imaging of actin protein from HeLa cells immunolabeled with phalloidin-conjugated nanoparticles under 852 nm irradiation and line profile analyses of the dotted line. Adapted with permission from Ref. [90], copyright by Springer (2022). (d) Wide-field (left) and super-resolution (right) images of the 4% Tm-doped UCNPs. Scale bar: 2  $\mu\text{m}$ , line profiles of two UCNPs. The diameter of the UCNPs is 40 nm (confirmed by TEM). Reconstruction processes were performed with fairSIM (an open-source image reconstruction solution for super-resolution SIM). (e) Evaluation of the image resolving power of upconversion SIM through thick mouse liver tissue, the comparison of images of the specimen by Wiener deconvolution and U-LSIM without covering the tissue slice. The scale bar is 2  $\mu\text{m}$ . (d, e) Adapted with permission from Ref. [86], copyright by American Chemical Society (2020) (color online).

## 4.2 Energy state manipulation for lifetime detection

The unique  $4f^N$  intraconfigurational transitions of lanthanide ions lead to long lifetimes, spanning from microseconds to milliseconds. According to J-O theory, the radiative lifetime can be calculated using the absorption spectrum and related parameters. However, the actual luminescence lifetime deviates from the radiative lifetime due to the participation of nonradiative decay and energy transfer processes between lanthanide ions or other species such as host matrices, surface defects, surface ligands, and exterior molecules. To

clarify this complexity, we categorize the manipulation of luminescent lifetime into three approaches: changing the crystal field and orbital hybridization, changing the energy diffusion distance, and introducing competing energy transfer pathways.

### 4.2.1 Changing the crystal field and orbital hybridization

Surface quenching through energy migration is a major factor for low luminescence efficiency [128,129]. By specifically selecting coordination molecules, our group enhanced the emission lifetime of  $\text{NaGdF}_4:\text{Yb/Tm}$

nanoparticles from 93 to 289  $\mu\text{s}$  ( $\text{Tm}^{3+}$ ) by attaching pyridine-2-carboxylic acid to nanoparticle surfaces [105]. This improvement is due to the reconstruction of orbital hybridization and crystal-field splitting, reducing the energy difference between surface and inner  $\text{Yb}^{3+}$  ions and facilitating energy migration.

#### 4.2.2 Changing the energy diffusion rate

The energy diffusion rate can be systematically modulated by varying the lanthanide doping concentration or by introducing shells of controllable thickness (Figure 2). In 2014, Jin and coworkers [92] proposed a multiplexing lifetime system for anticounterfeiting by increasing the  $\text{Tm}^{3+}$  dopant concentration from 0.2 mol% to 8 mol%. As a result of changes in energy transfer rate between  $\text{Yb}^{3+}$  and  $\text{Tm}^{3+}$ , and the cross relaxation rate of  $\text{Tm}^{3+}$ , the lifetime was decreased from 662 to 25.6  $\mu\text{s}$ . Our group developed a binary temporal coding method for anticounterfeiting applications by incorporating  $\text{Mn}^{2+}$  with a 39-ms lifetime into  $\text{NaGdF}_4:\text{Yb}/\text{Tm}$  UCNPs [130].

Changing the dopant ratio directly inevitably decreases luminescence at both ends of the lifetime tuning range. To avoid this, an energy migration layer can be designed to modulate the rise time and lifetime. Apart from the theoretical work discussed in Section 2 [68], Zhang and coworkers [84] also proposed a Yb-based energy relay layer to control the energy transfer time between  $\text{Nd}^{3+}$  and  $\text{Er}^{3+}$  in a multi-

layer, NIR-II emitting nanoparticle. This allows for lifetime tuning from 1.25 to 20.9 ms, providing multiple lifetime channels for detecting biomarker expression in tumors *in vivo*.

Apart from using time gating for lifetime imaging, Li and coworkers [112] found that a well-designed time gate can be used to separate excitation and emission spectra, even in the same band. As a proof, lanthanide emissions from singly doped  $\text{Yb}^{3+}$ ,  $\text{Nd}^{3+}$ ,  $\text{Tm}^{3+}$ , and  $\text{Er}^{3+}$  nanocrystals were detected within the same excitation band using ultrasmall  $\text{NaYbF}_4@$   $\text{CaF}_2$  nanoparticles. These nanoparticles have high emission brightness and tunable lifetimes (0.033 to 2.2 ms) that can be adjusted by changing the  $\text{CaF}_2$  shell thickness (0 to 5.3 nm). The  $\text{CaF}_2$  shell protects  $\text{Yb}^{3+}$  from non-radiative quenching by surface defects and ligands.

The energy diffusion path can also be blocked to produce orthogonal excitation and emission. Using inert shells to separate  $\text{Tm}^{3+}$ ,  $\text{Tb}^{3+}$ , and  $\text{Er}^{3+}$  dopants, Yan and coworkers [110] created a multi-compartment core-shell structure that allows orthogonal upconversion from activators under different excitation wavelengths (808 and 980 nm). This technique is particularly useful for anticounterfeiting in both spectral and lifetime domains.

#### 4.2.3 Introducing competing energy transfer pathways

Using time-gated methods, lanthanide-doped nanoparticles (LnNPs) with long luminescence lifetimes have been used in

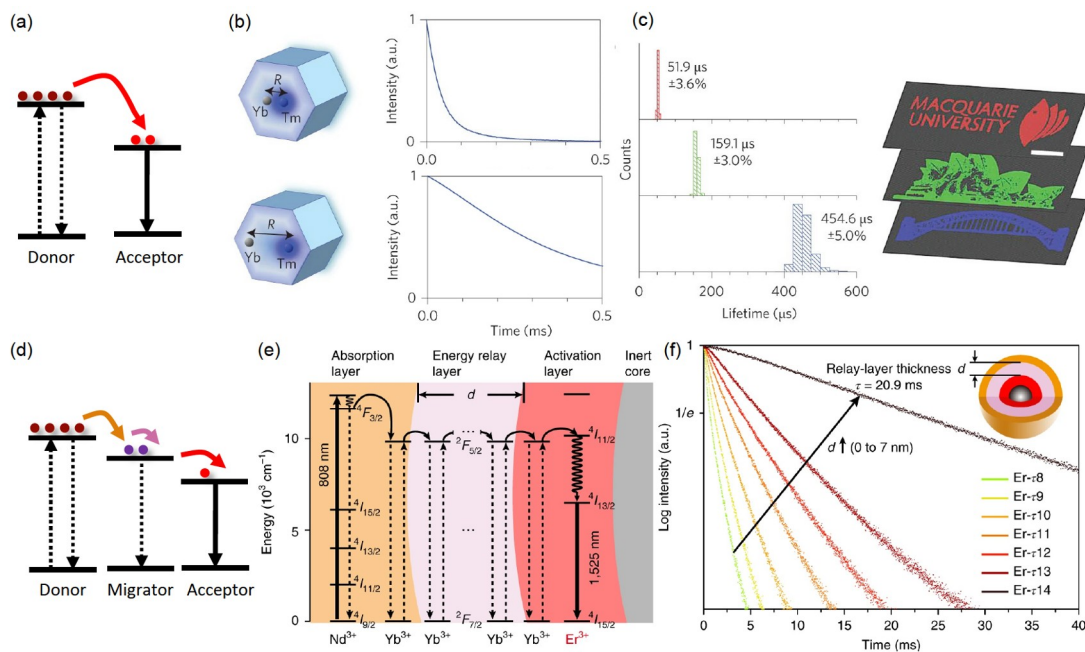


**Figure 2** Manipulation of lanthanide energy states for lifetime-based detection by controlling the energy diffusion rate. (a) Schematic of an energy transfer process. The energy transfer rate can be controlled by changing the dopant distance. (b) Schematic of lifetime tuning of  $\text{NaYF}_4:\text{Yb}/\text{Tm}$  nanocrystals ( $\tau$ -dots). (c) Time-resolved scanning showing pattern separation based on the lifetime components of every pixel containing different  $\text{Tm}$   $\tau$ -dots. (b, c) Adapted with permission from Ref. [92], copyright by Springer (2014). (d) Schematic of a migration layer inserted in the crystal for energy transfer, extending the overall transfer time. (e) Energy level diagram illustrating the luminescence process of multilayer nanoparticles. (f) Luminescence decay curves measured for Er nanoparticles at 1,525 nm with energy relay shells varying in thickness  $d$  from 0 to 7 nm (identical composition). (e, f) Adapted with permission from Ref. [84], copyright by Springer (2018) (color online).



Three typical strategies for constructing microlasers using UCNP are LSPR, whispering-gallery-mode (WGM) and Fabry-Perot (FP) cavity [138–140], which are discussed in this section (Figure 4).

The use of LSPR can improve the upconversion process by locally enhancing electromagnetic fields within sub-diffraction volumes. At metal-dielectric interfaces, free electrons oscillate collectively upon photon excitation, generating an electromagnetic field that boosts both the excitation process and emission intensity, and shortens the emission lifetime. It is possible to modulate luminescence dynamics by using electromagnetic fields generated by surface plasmonic arrays based on diffraction in a periodic structure to achieve sharp photonic modes [141,142]. Our group reported an upconversion superburst strategy with directional, fast, and ul-

trabright luminescence by coupling gap plasmon modes to nanoparticle emitters [140]. In a nanocavity consisting of a silver nanocube-coupled gold mirror structure, UCNP can experience substantial acceleration of their spontaneous emission and significant luminescence enhancement. The strong coupling of the nanocavity and the nanoparticle leads to more than 10,000-fold enhancement of spontaneous emission and 166-fold acceleration of spontaneous emission compared with control samples without nanocavity. Another approach to achieve LSPR is to coat UCNP onto metal nanopillars, as demonstrated by Odom's group [143] using Ag nanopillar arrays conformally coated with  $\text{Yb}^{3+}/\text{Er}^{3+}$ -doped UCNP. The nanocavity achieved stable lasing at room temperature with lasing thresholds as low as  $29 \text{ W cm}^{-2}$ . In contrast to conventional UCNP with a

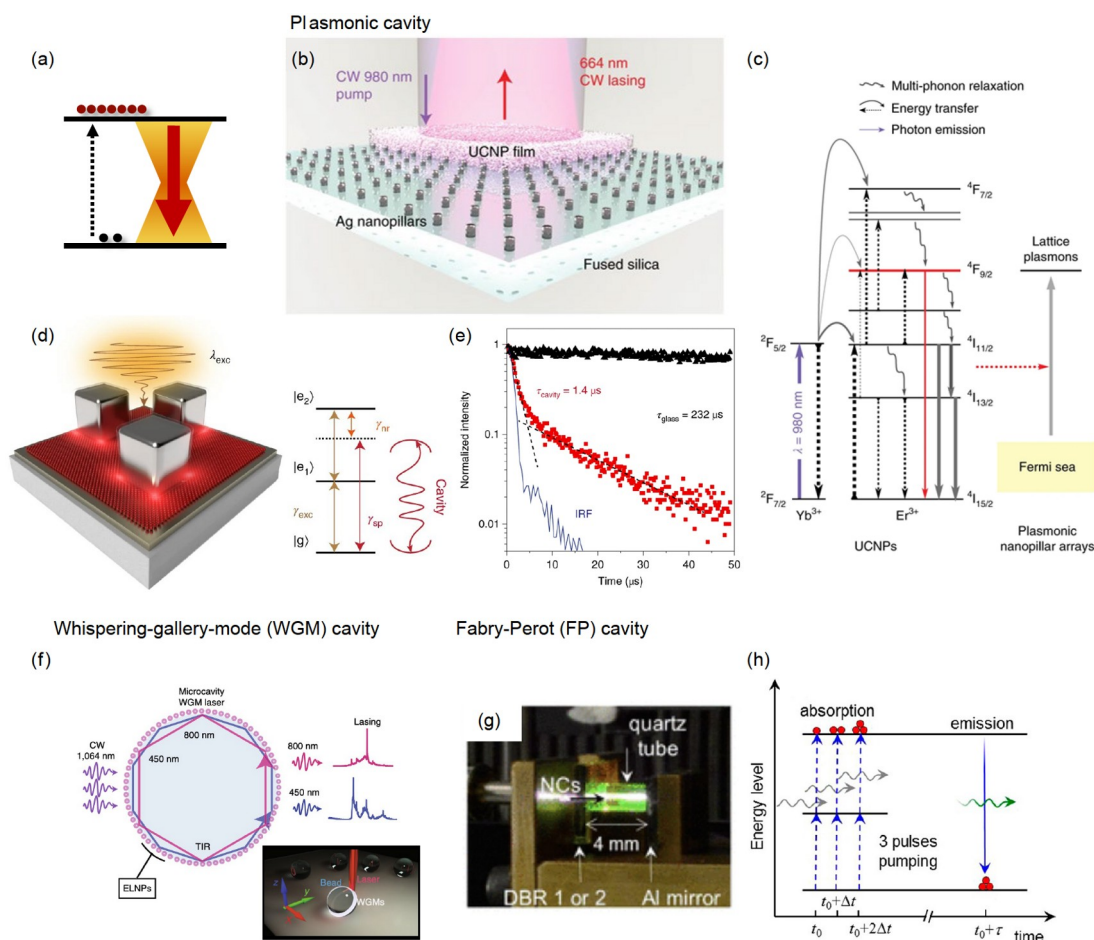


**Figure 4** Manipulation of lanthanide energy states in an enhanced electromagnetic field. (a) Simplified schematic of a cavity-coupled energy pumping process. The luminescence dynamics are changed by the enhanced electromagnetic field. (b) Schematic of UCNPs coating on Ag arrays with a spacing of  $a_0 = 450 \text{ nm}$ . (c)  $\text{Yb}^{3+}/\text{Er}^{3+}$  energy levels and coupling mechanism with lattice plasmons. (b, c) Adapted with permission from Ref. [143], copyright by Springer (2019). (d) Plasmonic cavity-coupled UCNP comprising a gold thin film, a silver nanocube, and a monolayer of UCNP embedded in the sub-20-nm gap (left) and simplified energy-level diagram describing the ESA-mediated upconversion process (right). (e) Comparison of the normalized time-resolved luminescence decay for UCNP deposited on a glass slide (black) and UCNP enhanced by the nanocavity mode (red) at an emission wavelength of 660 nm. (d, e) Adapted with permission from Ref. [140], copyright by Springer (2019). (f) Schematic of the excitation and lasing in a microbead coated with  $\text{Tm}^{3+}$ -doped energy-looping nanoparticles (ELNPs). TIR, total internal reflection. Inset: 3D representation of lasing WGMs in the microsphere. Adapted with permission from Ref. [146], copyright by Springer (2018). (g) Image of the FP cavity using  $\text{NaYF}_4:\text{Yb}/\text{Er}/\text{NaYF}_4$  nanocrystals dispersed in cyclohexane as the gain medium. (h) Schematic of dynamic population alignment under 3-pulse laser excitation with 10 ns delay. (g, h) Adapted with permission from Ref. [139], copyright by American Chemical Society (2013) (color online).

spontaneous emission lifetime of around 100  $\mu\text{s}$ , nanopillar-coupled nanoparticles showed lasing emission at 660 nm in a 1- $\mu\text{s}$  time window with a slow component of 510 ns and a fast component of 66 ns according to a bi-exponential fit. LSPR is a powerful tool for producing lasers by radically shifting the electromagnetic environment of UCNPs and modulating their emission characteristics without affecting composition, size, or morphology.

WGM cavities are microspheres with closed-loop light paths guided by total internal reflection at their surface, leading to low-power lasing. These cavities, with a variety of shapes such as bottles, spheres, toroids and rings, are ideal for microlasers due to their high quality factors and small mode volumes [144]. Yu's group [145] demonstrated white-light lasing at room temperature from a  $\text{Yb}^{3+}\text{-Er}^{3+}\text{-Tm}^{3+}$  tri-doped hexagonal  $\beta\text{-NaYF}_4$  microrod with WGM resonance. The number and wavelength of amplified modes can be selected by modulating the diameter of microspheres. To simultaneously excite RGB lasing within the same microcavity, the radius of the microrods was set to 4  $\mu\text{m}$  so that all RGB WGMs had a similar range of threshold power. In Schuck's work [146], the polystyrene WGM cavity was designed with a diameter of 5  $\mu\text{m}$  to ensure that both transverse electric and magnetic propagation modes had high quality factors. The use of microscale lasers offers the potential for new technologies specifically tailored for operation in confined spaces, such as ultra-high-speed microprocessors and live brain tissue. In contrast, conventional microbubbles and microfibers have unpredictable sizes due to limitations in reflow and thermal drawing techniques, making it difficult to control laser wavelengths and mode spacing.

FP cavity is employed in photonic chips to generate lasers with low threshold current and decent output power [147]. In a classic Fabry-Perot cavity, two closely spaced, partially reflecting mirrors form a resonant optical cavity to transmit light at wavelengths that are multiples of the mirror spacing at small incident angles [148]. An optical resonance occurs when the optical path length reaches an integer multiple of the light wavelength. Yu and coworkers [139] first realized amplified spontaneous emission from an FP cavity consisting of a quartz tube between a distributed Bragg reflector and an Al mirror containing  $\text{NaYF}_4\text{:Yb/Er@NaYF}_4$  nanoparticles, with three narrowing emission bands. However, the long cavity length prevents fine structures of the lasing spectra from being observed.

While most contemporary studies have successfully measured considerable changes in emission intensity or decay rate, targeting the emission performance to a desired spectral or temporal range remains a challenge. Achieving complex laser modes and operations using typical lanthanide nanoparticles has not yet been realized. As discussed in Section 2.2, designing and simulating kinetic models in conjunction

with multi-parameter electromagnetic fields can serve as an indispensable tool to overcome these challenges.

#### 4.4 X-ray persistent luminescence

Persistent luminescence, which can be activated by X-rays, is important for information storage, security encryption, bioimaging, and biosensing [149,150]. Mechanistic investigations have shown that large bandgaps, host materials with heavy atoms, and lattice defects are important factors that improve performance. Lanthanide ions are commonly used to generate persistent luminescence because they offer great optical tunability in terms of emission wavelength and lifetime, thanks to their intraconfigurational 4f-4f and interconfigurational 4f-5d transitions [151].

An example of persistent scintillation in the visible and UV range is  $\text{NaLuF}_4\text{:Tb}^{3+}\text{@NaYF}_4$  nanoscintillators, which continue to emit visible radioluminescence for more than 30 days after X-ray cessation (Figure 5) [114]. Furthermore, multicolor modulation of radioluminescence from the UV-Vis to the NIR region was also demonstrated in this work. In the UV range, the emission in ultraviolet C (UVC) (200–280 nm) was achieved using a defect-bearing fluoride elpasolite ( $\text{Cs}_2\text{NaYF}_6$ ) as the host and  $\text{Pr}^{3+}$  ions as emitters [152]. Longer wavelengths can penetrate deeper into the tissue and improve contrast. Recent work has extended the emission band into NIR-II (1,000–1,400 nm) and NIR-III (1,500–1,800 nm) biological windows. Zhang's group [115] recently developed UCNPs with an emission wavelength in the NIR-II window using  $\text{NaY(Gd)F}_4$  with low phonon energy as the host material and  $\text{Nd}^{3+}$ ,  $\text{Ho}^{3+}$ ,  $\text{Tm}^{3+}$ , or  $\text{Er}^{3+}$  dopants as activators. The host matrix and core-shell architecture are crucial for optimizing the scintillation. The host material must have a large bandgap and readily generate anionic defects, while the core-shell design must minimize surface and concentration quenching effects. Fluoride crystals are considered good candidates because they can easily generate anionic defects [152].

In addition to spectroscopy, the dynamics of persistent luminescence were also utilized to mimic synaptic behavior [153].  $\text{CaAl}_2\text{O}_4\text{:0.5%Eu}^{2+}$  phosphors can simulate short-term potentiation of the synapse by lower frequency and more excitation pulses, while higher frequency and reduced number of pulses lead to long-term potentiation. A model of seed-centered electron-coupled trap clustering was proposed to explain the change in dynamics of persistent luminescence.

Although persistent emission has already covered a wide range of topics summarized in previous examples, there is still no universal way to describe the whole mechanism for a given persistent phosphor [80,154–156]. However, all existing models agree that persistent luminescence depends heavily on the bandgap and defects in the host matrix. The

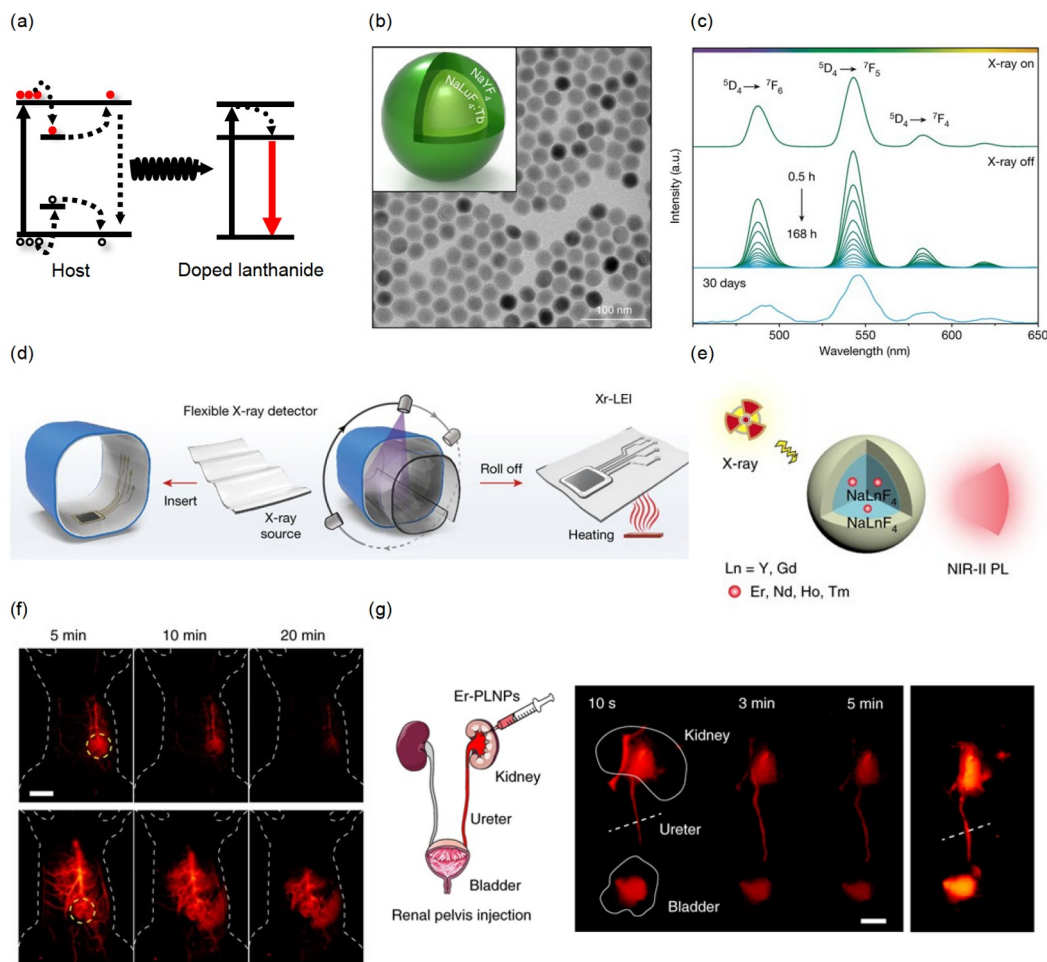


**Figure 5** Mechanism and applications of X-ray persistent luminescence. (a) Proposed mechanism of long-lived persistent radioluminescence of lanthanide-doped nanocrystals. Upon X-ray excitation, electrons are photoexcited in an inner electronic shell of lattice atoms to produce low-energy electrons, which are either transferred to activators for emission or partially stored in traps. Electrons in shallow traps are slowly released for spontaneous long-lasting emission. In contrast, electrons in deep traps populate to the conduction band (CB) under optical or thermal stimulation. VB, valence band. (b) TEM micrograph of NaLuF<sub>4</sub>:Tb (15 mol%)/NaYF<sub>4</sub> nanocrystals. (c) Radioluminescence emission spectra of the core-shell nanocrystals, recorded after cessation of X-rays (50 kV) for 0.5–168 h or 30 days. (d) Schematic showing 3D electronic imaging enabled by a nanoscintillator-integrated, flexible detector. (b–d) Adapted with permission from Ref. [114], copyright by Springer (2021). (e) Schematic of X-ray-activated persistent luminescence (PL) generated in lanthanide-doped nanoparticles. (f) Time-dependent NIR-II persistent luminescence (top) and NIR-II luminescence (bottom) images of tumors in living mice after multiple injections of Er-doped persistent luminescence nanoparticles (Er-PLNPs). Scale bar, 1 cm. (g) Time-dependent NIR-II PL (centre) and NIR-II luminescence (right) images of a ureter in a living mouse after renal pelvic injection of Er-PLNPs (left). The FWHM of the ureter is smaller in PL images. (e–g) Adapted with permission from Ref. [115], copyright by Springer (2021) (color online).

design strategy is increasingly focused on addressing the following questions: is the bandgap large enough to accommodate desired traps; is the concentration of defects sufficient to store the radiative energy; and are the defects in the matrix effectively involved in the charge carrier trapping process? In a recent study by Xu and coworkers [157], the inclusion of interstitial Na<sup>+</sup> ions within NaLuF<sub>4</sub>:Gd-based nanoparticles was utilized to enhance persistent luminescence intensity. Upon X-ray irradiation, interstitial Na<sup>+</sup> ions formed anion-Frenkel defects, which contributed to trap formation and enhanced luminescence. To fully understand the phenomenon, it is important to examine the underlying mechanisms of X-ray-activated persistent luminescence.

## 4.5 Other notable applications

### 4.5.1 3D printing

Additive manufacturing, also known as 3D printing, allows the fabrication of geometrically complex and functional structures by combining nanomaterials with the process [158]. This method overcomes the limitations of conventional manufacturing and produces structures with high geometric complexity and multifunctionality that can be modified spatially and temporally [159]. The integration of nanomaterials with 3D printing also enables the tuning of functional properties at both the nanoscale and macroscale.

Recent technological advances have enabled the integration of lanthanide-doped photonic materials with 3D print-

ing. This combination is used to fabricate photonic devices and 3D materials by combining lanthanides with 3D-printable polymers. A typical example is the recently published work by Wu and coworkers [160], in which 3D assembly of luminescent lanthanide MOFs was controlled by additive manufacturing and subsequent post-printing treatment. They selected an alginate-containing formulation as the precursor ink to print the structure by direct ink writing. After immersion in a solution of lanthanide MOFs,  $\text{Eu}^{3+}$  ions and EuMOFs were uniformly decorated on the surface and interior of sodium alginate. This was achieved by exerting traction forces to drive the alginate outward and then chelating with the ions. However, precise control of the ligand content is necessary to avoid interfering with the printing process and assembly.

Alternatively, integrating lanthanide ions into the ink can realize 3D printing of photonic devices without post-treatment [161,162]. Tang and coworkers [162] reported polyelectrolyte-stabilized nanoparticles with the inclusion of  $\text{Ln}^{3+}$  complexes, in which the positively charged  $\text{Ln}^{3+}$  ions interact electrostatically with negatively charged substituents of polyelectrolyte chains and induce aggregation to form nanostructures. They then integrated the stabilized nanoparticles into a poly (lactic acid) matrix as the printing material [162]. Other materials can also be used as printing media, such as hydrogels, which offer a combination of biological and luminescent properties. For instance, Zhou and coworkers [163] developed a shape- and color-responsive hydrogel ink that responded to different humidity or hydration/dehydration. The printable ink consisted of  $\text{Eu}^{3+}$ -coordinated zwitterionic polyethyleneimine-co-poly (acrylic acid) (PEI-co-PAA) copolymers and poly(ethylene glycol) diacrylate (PEGDA), achieving controllable fluorescent colors based on the competing effect between blue-green emitting PEI-co-PAA copolymers and red emitting lanthanide  $\text{Eu}^{3+}$  ions.

UCNPs have been used as ultraviolet activators for photoinitiation in direct 3D printing processes. They take advantage of NIR-triggered emission to enable deep 3D photopolymerization without the need for layer-by-layer printing. For example, Méndez-Ramos and coworkers [164] demonstrated NIR-activated 3D structure formation in photocurable organic base resin. The radiation power and exposure time were greatly reduced compared to simultaneous two-photon absorption techniques. Khaydukov and coworkers [165] further investigated the polymerization process at both millimeter and sub-micrometer scales. The anisotropy of nanoparticles led to different polymerization rates between the flat surface and the edge, thus determining the printing resolution.

In addition to laser scanning lithography, a projection method based on digital mirror devices has also been used in 3D bioprinting [166]. Using UCNPs as nano-initiators, the

injected bio-ink was printed into customized tissue constructs *in situ* and *in vivo*. However, the luminescence properties of the printed products were not fully considered.

To summarize, 3D printing is a powerful tool for developing large-scale photonic devices using lanthanide-based materials. Challenges remain in the integration of controlled micro/nanoform and photonic properties, as well as in the fabrication of tailored materials for biological, photonic and telecommunication applications.

#### 4.5.2 Optogenetics

Optogenetics is a field that uses optical stimuli to manipulate cellular and neuronal activities. UCNPs, which can be optically excited by NIR light, are becoming a popular choice as probes for optogenetics. This is due to their plentiful visible emission bands, excellent photostability, and good biocompatibility. The ability of UCNPs to be excited by NIR light sets them apart from other fluorescent probes such as green fluorescent protein. NIR light causes minimal scattering and absorption in tissue, allowing deep penetration and a better signal-to-noise ratio compared with other probes.

The first application of UCNPs in optogenetics can be traced back to 2015 when Yawo and coworkers [167] used  $\text{NaYF}_4:\text{Sc}/\text{Yb}/\text{Er}$  nanoparticles to sensitize 975 nm excitation and create green emission that was matched with the absorption of ChR2, resulting in the stimulation of ND7/23 cells expressing C1-V1. To further enhance NIR absorption, Han and coworkers [168] designed dye-sensitized (IR-806)  $\text{NaYF}_4:\text{Yb}/\text{Er}@/\text{NaYF}_4:\text{Yb}$  UCNPs, with efficient optical activation at 800 nm for ReaChR in cultured hippocampal neurons.

In 2017, Shi and coworkers [169] designed a UCNP-based transducer by packing Er- or Tm-doped UCNPs at high concentration into a glass microoptrode and implanting it into a live rodent's brain. The nanoparticles, located near neurons expressing ChR2 or C1V1, converted NIR light into visible emission for optical stimulation of these opsin proteins. In a separate *in vivo* application, McHugh and coworkers [170] injected  $\text{NaYF}_4:\text{Yb}/\text{Tm}$  UCNPs into the ventral tegmental area to stimulate neuronal activity with Tm emission under 980 nm excitation.

Although UCNPs have shown promising performance as *in vivo* optical probes due to their NIR excitability, they still have a low intrinsic quantum yield (typically below 1%). Future UCNP-based optogenetic devices should enhance emission intensity while avoiding severe heating effects on tissue, as emission intensity appears to be positively correlated with excitation power.

## 5 Summary and outlook

Over the last 20 years, research in lanthanide photonics has

rapidly grown, leading to advances in material design, bioimaging and sensing, super-resolution imaging, lasing and many other fields. However, some bottlenecks still hinder wide applications of lanthanide-doped materials [171]. We have summarized some of them for discussion.

(1) Bioconjugation for bioimaging and point-of-care testing (POCT). For imaging applications, bioconjugation of lanthanide nanomaterials to biomolecules has made great progress. However, there are still challenges in developing stable and widely applicable fluorescent probes compared to older generations such as organic dyes, quantum dots, and nanodiamonds. Furthermore, for *in vivo* imaging and therapeutic applications, the biosafety of lanthanide materials has always been a concern. For commercial POCT applications, lanthanide materials remain promising candidates, but their industrial-grade synthesis and modification techniques remain unexplored.

(2) Limitations in material constructions. The commonly used fluoride crystal is optimized for low phonon energy and best luminescence intensity. However, this sodium fluoride matrix also limits wider applications of lanthanide emission. The fluoride-containing surface reduces bioaffinity to molecules. It also complicates the morphological transformation of materials (*e.g.*, flexible nanowires, ribbons, large spheres). Future uses will demand a wider variety of materials. Lanthanide-based materials, including complexes, polymers, MOFs, and conjugates with peptides, proteins, RNA and DNA, could be the direction of future development.

(3) Limitations of expensive and sophisticated instrumentation. Super-resolution systems, including SIM and STED systems, are currently high-end laboratory systems that need major customization. Technology adoption has been restricted by expensive components and sophisticated software development. It is hoped that emerging demands in 3D vision, laser radar, display and projection, image recognition, and algorithm-based super-resolution will lead to more affordable, commercial-grade components and algorithms.

With the theories, tools and applications discussed above, energy level manipulation plays a key role in lanthanide research. Further possibilities for energy manipulation are discussed below.

(1) Theory and technology development and standardization. One possible solution is open-source packages for some of the widely used theories and technologies. This will greatly lower the difficulty of entering the field. Sharing elementary tools will enable evaluation of different methods. This will further accelerate the field while leveraging all existing knowledge and techniques.

(2) Taking advantage of state-of-the-art optical technologies. Because of advances in investigative tools, test conditions have changed dramatically. Research priorities have shifted from relatively low excitation power to high power

conditions, from a steady state to a temporal state, and from a cluster or solution to a single particle or even a single photon. These conditions help the discovery of novel photonic applications such as single photon sources, ultrafast lifetime imaging microscopy, single-ion catalysis with single-molecule fluorescence or electrochemical methods. Incontrovertibly, lanthanide research can be advanced by using state-of-the-art optical technologies in physical, chemical and biological fields (*e.g.*, quantum optics, single ion catalysis, neuron studies).

(3) Extended energy range. Currently, most studies are conducted within the UV and visible wavelength range. However, there have been recent studies in exploring the near-infrared range. To further explore the potential of lanthanide emission, future studies could focus on the vacuum ultraviolet (photoelectron spectroscopy, photolithography), mid-infrared (molecular sensing, thermal imaging, and telecommunications), and terahertz regions (security screening, non-destructive testing, and ultrafast communication).

(4) Integration into chips and devices. The development of optical chips and devices that take advantage of the excellent optical properties of lanthanide photonic materials requires collaboration across various fields. Although there is limited room for basic science exploration, advances in technology can also provide valuable knowledge for designing application-oriented materials [172].

**Acknowledgements** This work was supported by the National Research Foundation, the Prime Minister's Office of Singapore under its Competitive Research Program (NRF-CRP23-2019-0002) and NRF Investigatorship Programme (NRF-NRFI05-2019-0003), the RIE2025 Manufacturing, Trade and Connectivity (MTC) Programmatic Fund (M21J9b0085), and the King Abdullah University of Science and Technology (KAUST) Office of Sponsored Research (OSR-2018-CRG7-3736).

**Conflict of interest** The authors declare no conflict of interest.

- 1 Becquerel J, Onnes HK. The absorption spectrums of lanthanide crystals and their modification in an electrical field at the temperatures of liquefaction and solidification of hydrogen. *C R Hebd Seances Acad Sci*, 1908, 146: 625–628
- 2 Levine AK, Palilla FC. *Appl Phys Lett*, 1964, 5: 118–120
- 3 Auzel F. *J Lumin*, 2020, 223: 116900
- 4 Auzel F. *Chem Rev*, 2004, 104: 139–174
- 5 Menyuk N, Dwight K, Pierce JW. *Appl Phys Lett*, 1972, 21: 159–161
- 6 Auzel FE. *Proc IEEE*, 1973, 61: 758–786
- 7 Johnson LF, Guggenheim HJ. *Appl Phys Lett*, 1971, 19: 44–47
- 8 Wright JC, Zalucha DJ, Lauer HV, Cox DE, Fong FK. *J Appl Phys*, 1973, 44: 781–786
- 9 Piper WW, DeLuca JA, Ham FS. *J Lumin*, 1974, 8: 344–348
- 10 Sommerdijk JL, Bril A, de Jager AW. *J Lumin*, 1974, 8: 341–343
- 11 Matsuzawa T, Aoki Y, Takeuchi N, Murayama Y. *J Electrochem Soc*, 1996, 143: 2670–2673
- 12 Murray CB, Norris DJ, Bawendi MG. *J Am Chem Soc*, 1993, 115: 8706–8715
- 13 Alivisatos AP. *Science*, 1996, 271: 933–937
- 14 Bruchez Marcel J, Moronne M, Gin P, Weiss S, Paul Alivisatos A. *Science*, 1998, 281: 2013–2016
- 15 Wang X, Zhuang J, Peng Q, Li Y. *Nature*, 2005, 437: 121–124

- 16 Heer S, Kömpe K, Güdel HU, Haase M. *Adv Mater*, 2004, 16: 2102–2105
- 17 Mai HX, Zhang YW, Si R, Yan ZG, Sun L, You LP, Yan CH. *J Am Chem Soc*, 2006, 128: 6426–6436
- 18 Li Z, Zhang Y. *Nanotechnology*, 2008, 19: 345606
- 19 Wang L, Li Y. *Chem Mater*, 2007, 19: 727–734
- 20 Wang F, Han Y, Lim CS, Lu Y, Wang J, Xu J, Chen H, Zhang C, Hong M, Liu X. *Nature*, 2010, 463: 1061–1065
- 21 Wang F, Deng R, Wang J, Wang Q, Han Y, Zhu H, Chen X, Liu X. *Nat Mater*, 2011, 10: 968–973
- 22 Wang F, Liu X. *J Am Chem Soc*, 2008, 130: 5642–5643
- 23 Li Z, Zhang Y, Jiang S. *Adv Mater*, 2008, 20: 4765–4769
- 24 Chen G, Qiu H, Prasad PN, Chen X. *Chem Rev*, 2014, 114: 5161–5214
- 25 Zhou J, Liu Q, Feng W, Sun Y, Li F. *Chem Rev*, 2015, 115: 395–465
- 26 Zhou J, Liu Z, Li F. *Chem Soc Rev*, 2012, 41: 1323–1349
- 27 Vetrone F, Naccache R, Zamarrón A, Juarranz de la Fuente A, Sanz-Rodríguez F, Martínez Maestro L, Martín Rodríguez E, Jaque D, García Solé J, Capobianco JA. *ACS Nano*, 2010, 4: 3254–3258
- 28 Idris NM, Gnanasammandhan MK, Zhang J, Ho PC, Mahendran R, Zhang Y. *Nat Med*, 2012, 18: 1580–1585
- 29 Wang YF, Liu GY, Sun LD, Xiao JW, Zhou JC, Yan CH. *ACS Nano*, 2013, 7: 7200–7206
- 30 Dong H, Du SR, Zheng XY, Lyu GM, Sun LD, Li LD, Zhang PZ, Zhang C, Yan CH. *Chem Rev*, 2015, 115: 10725–10815
- 31 Zou W, Visser C, Maduro JA, Pshenichnikov MS, Hummelen JC. *Nat Photon*, 2012, 6: 560–564
- 32 van der Ende BM, Aarts L, Meijerink A. *Phys Chem Chem Phys*, 2009, 11: 11081–11095
- 33 Zhou B, Shi B, Jin D, Liu X. *Nat Nanotech*, 2015, 10: 924–936
- 34 Wang L, Yan R, Huo Z, Wang L, Zeng J, Bao J, Wang X, Peng Q, Li Y. *Angew Chem Int Ed*, 2005, 44: 6054–6057
- 35 Zheng W, Huang P, Tu D, Ma E, Zhu H, Chen X. *Chem Soc Rev*, 2015, 44: 1379–1415
- 36 Bogdan N, Vetrone F, Ozin GA, Capobianco JA. *Nano Lett*, 2011, 11: 835–840
- 37 Dieke GH, Crosswhite HM. *Appl Opt*, 1963, 2: 675–686
- 38 Judd BR. *Phys Rev*, 1962, 127: 750–761
- 39 Ofelt GS. *J Chem Phys*, 1962, 37: 511–520
- 40 Hehlen MP, Brik MG, Krämer KW. *J Lumin*, 2013, 136: 221–239
- 41 Walsh BM. Judd-Ofelt theory: principles and practices. In: Di Bartolo B, Forte O, Eds. *Advances in Spectroscopy for Lasers and Sensing*. Betherlands: Springer, 2006. 403–433
- 42 Carnall WT, Fields PR, Rajnak K. *J Chem Phys*, 1968, 49: 4424–4442
- 43 Goldner P, Auzel F. *J Appl Phys*, 1996, 79: 7972–7977
- 44 Levey CG, Glynn TJ, Yen WM. *J Lumin*, 1984, 31–32: 245–247
- 45 Levey CG. *J Lumin*, 1990, 45: 168–171
- 46 Quimby RS, Miniscalco WJ. *J Appl Phys*, 1994, 75: 613–615
- 47 Merkle LD, Zandi B, Moncorgé R, Guyot Y, Verdun HR, McIntosh B. *J Appl Phys*, 1996, 79: 1849–1856
- 48 Smentek L. *Phys Rep*, 1998, 297: 155–237
- 49 McCumber DE. *Phys Rev*, 1964, 136: A954–A957
- 50 Payne SA, Chase LL, Smith LK, Kway WL, Krupke WF. *IEEE J Quantum Electron*, 1992, 28: 2619–2630
- 51 Zou X, Toratani H. *J Non-Crystalline Solids*, 1996, 195: 113–124
- 52 Su LB, Wang QG, Li HJ, Brasse G, Camy P, Doualan JL, Braud A, Moncorgé R, Zhan YY, Zheng LH, Qian XB, Xu J. *Laser Phys Lett*, 2013, 10: 035804
- 53 Brenier A, Boulon G. *J Alloys Compd*, 2001, 323–324: 210–213
- 54 Hu JY, Ning Y, Meng YS, Zhang J, Wu ZY, Gao S, Zhang JL. *Chem Sci*, 2017, 8: 2702–2709
- 55 Hasegawa M, Ohmagari H, Tanaka H, Machida K. *J Photochem Photobiol C-Photochem Rev*, 2022, 50: 100484
- 56 Demirbas U, Thesinga J, Kellert M, Kärtner FX, Pergament M. *Opt Mater Express*, 2021, 11: 250–272
- 57 Haumesser PH, Gaumé R, Viana B, Antic-Fidancev E, Vivien D. *J Phys-Condens Matter*, 2001, 13: 5427–5447
- 58 Haumesser PH, Gaume R, Viana B, Vivien D. *J Opt Soc Am B*, 2002, 19: 2365–2375
- 59 Kong M, Gu Y, Chai Y, Ke J, Liu Y, Xu X, Li Z, Feng W, Li F. *Sci China Chem*, 2021, 64: 974–984
- 60 Weber MJ. *Phys Rev B*, 1971, 4: 3153–3159
- 61 Jaque D, Ramirez MO, Bausá LE, Solé JG, Cavalli E, Speghini A, Bettinelli M. *Phys Rev B*, 2003, 68: 035118
- 62 Dexter DL. *J Chem Phys*, 1953, 21: 836–850
- 63 Kushida T. *J Phys Soc Jpn*, 1973, 34: 1318–1326
- 64 Malta OL. *J Non-Crystalline Solids*, 2008, 354: 4770–4776
- 65 Carneiro Neto AN, Moura Renaldo T. J, Malta OL. *J Lumin*, 2019, 210: 342–347
- 66 Yamada N, Shionoya S, Kushida T. *J Phys Soc Jpn*, 1972, 32: 1577–1586
- 67 Ramirez MO, Jaque D, Bausá LE, Martín IR, Lahoz F, Cavalli E, Speghini A, Bettinelli M. *J Appl Phys*, 2005, 97: 093510
- 68 Zuo J, Sun D, Tu L, Wu Y, Cao Y, Xue B, Zhang Y, Chang Y, Liu X, Kong X, Buma WJ, Meijer EJ, Zhang H. *Angew Chem Int Ed*, 2018, 57: 3054–3058
- 69 Tu LP, Zuo J, Zhang H. *Sci China Tech Sci*, 2018, 61: 1301–1308
- 70 Feng Y, Li Z, Li Q, Yuan J, Tu L, Ning L, Zhang H. *Light Sci Appl*, 2021, 10: 105
- 71 Xue B, Wang D, Tu L, Sun D, Jing P, Chang Y, Zhang Y, Liu X, Zuo J, Song J, Qu J, Meijer EJ, Zhang H, Kong X. *J Phys Chem Lett*, 2018, 9: 4625–4631
- 72 Purcell EM. *Phys Rev*, 1946, 69: 681–681
- 73 Pelton M. *Nat Photon*, 2015, 9: 427–435
- 74 Wang YZ, Lu BL, Li YQ, Liu YS. *Opt Lett*, 1995, 20: 770–772
- 75 Svelto O, Hanna DC. *Principles of Lasers*. New York: Springer, 1998
- 76 Silfvast WT. *Laser Fundamentals*. Cambridge: Cambridge University Press, 2004
- 77 Xiao G, Bass M. *IEEE J Quantum Electron*, 1997, 33: 41–44
- 78 Zayhowski JJ, Kelley PL. *IEEE J Quantum Electron*, 1991, 27: 2220–2225
- 79 Novelline RA, Squire LF. *Squire's Fundamentals of Radiology*. La Editorial, UPR: Harvard University Press, 1997
- 80 Suo H, Zhang X, Wang F. *Trends Chem*, 2022, 4: 726–738
- 81 Liu Q, Zhang Y, Peng CS, Yang T, Joubert LM, Chu S. *Nat Photon*, 2018, 12: 548–553
- 82 Yi Z, Gao H, Ji X, Yeo XY, Chong SY, Mao Y, Luo B, Shen C, Han S, Wang JW, Jung S, Shi P, Ren H, Liu X. *J Am Chem Soc*, 2021, 143: 14907–14915
- 83 Zheng X, Zhu X, Lu Y, Zhao J, Feng W, Jia G, Wang F, Li F, Jin D. *Anal Chem*, 2016, 88: 3449–3454
- 84 Fan Y, Wang P, Lu Y, Wang R, Zhou L, Zheng X, Li X, Piper JA, Zhang F. *Nat Nanotech*, 2018, 13: 941–946
- 85 Qiu X, Zhou Q, Zhu X, Wu Z, Feng W, Li F. *Nat Commun*, 2020, 11: 4
- 86 Liu B, Chen C, Di X, Liao J, Wen S, Su QP, Shan X, Xu ZQ, Ju LA, Mi C, Wang F, Jin D. *Nano Lett*, 2020, 20: 4775–4781
- 87 Wang F, Ma Z, Zhong Y, Salazar F, Xu C, Ren F, Qu L, Wu AM, Dai H. *Proc Natl Acad Sci USA*, 2021, 118: e2023888118
- 88 Denkova D, Ploschner M, Das M, Parker LM, Zheng X, Lu Y, Orth A, Packer NH, Piper JA. *Nat Commun*, 2019, 10: 3695
- 89 Lee C, Xu EZ, Liu Y, Teitelboim A, Yao K, Fernandez-Bravo A, Kotulska AM, Nam SH, Suh YD, Bednarkiewicz A, Cohen BE, Chan EM, Schuck PJ. *Nature*, 2021, 589: 230–235
- 90 Liang Y, Zhu Z, Qiao S, Guo X, Pu R, Tang H, Liu H, Dong H, Peng T, Sun LD, Widengren J, Zhan Q. *Nat Nanotechnol*, 2022, 17: 524–530
- 91 Wang F, Ren F, Ma Z, Qu L, Gourgues R, Xu C, Baghdasaryan A, Li J, Zadeh IE, Los JWN, Fognini A, Qin-Dregely J, Dai H. *Nat Nanotechnol*, 2022, 17: 653–660
- 92 Lu Y, Zhao J, Zhang R, Liu Y, Liu D, Goldys EM, Yang X, Xi P, Sunna A, Lu J, Shi Y, Leif RC, Huo Y, Shen J, Piper JA, Robinson JP, Jin D. *Nat Photon*, 2013, 8: 32–36

- 93 Zhou L, Fan Y, Wang R, Li X, Fan L, Zhang F. *Angew Chem*, 2018, 130: 13006–13011
- 94 Liang L, Feng Z, Zhang Q, Cong TD, Wang Y, Qin X, Yi Z, Ang MJY, Zhou L, Feng H, Xing B, Gu M, Li X, Liu X. *Nat Nanotechnol*, 2021, 16: 975–980
- 95 Liu Y, Lu Y, Yang X, Zheng X, Wen S, Wang F, Vidal X, Zhao J, Liu D, Zhou Z, Ma C, Zhou J, Piper JA, Xi P, Jin D. *Nature*, 2017, 543: 229–233
- 96 Cole RW, Jinadasa T, Brown CM. *Nat Protoc*, 2011, 6: 1929–1941
- 97 Jonkman J, Brown CM, Wright GD, Anderson KI, North AJ. *Nat Protoc*, 2020, 15: 1585–1611
- 98 Gao L, Shao L, Chen BC, Betzig E. *Nat Protoc*, 2014, 9: 1083–1101
- 99 Bacia K, Schwille P. *Nat Protoc*, 2007, 2: 2842–2856
- 100 Sun Y, Day RN, Periasamy A. *Nat Protoc*, 2011, 6: 1324–1340
- 101 Wang J, Allgeyer ES, Sirinakis G, Zhang Y, Hu K, Lessard MD, Li Y, Diekmann R, Phillips MA, Dobbie IM, Ries J, Booth MJ, Bewersdorf J. *Nat Protoc*, 2021, 16: 677–727
- 102 Sezgin E, Schneider F, Galiani S, Urbančić I, Waithe D, Lagerholm BC, Eggeling C. *Nat Protoc*, 2019, 14: 1054–1083
- 103 Birk UJ. *Super-resolution Microscopy. A Practical Guide*. Weinheim: John Wiley & Sons, 2017
- 104 Xi P, Rajwa B, Jones JT, Robinson JP. *Am J Phys*, 2007, 75: 203–207
- 105 Xu H, Han S, Deng R, Su Q, Wei Y, Tang Y, Qin X, Liu X. *Nat Photon*, 2021, 15: 732–737
- 106 Zhou J, Wen S, Liao J, Clarke C, Tawfik SA, Ren W, Mi C, Wang F, Jin D. *Nat Photon*, 2018, 12: 154–158
- 107 Liang L, Wang C, Chen J, Wang QJ, Liu X. *Nat Photon*, 2022, 16: 712–717
- 108 Zhan Q, Liu H, Wang B, Wu Q, Pu R, Zhou C, Huang B, Peng X, Ågren H, He S. *Nat Commun*, 2017, 8: 1058
- 109 Chen C, Wang F, Wen S, Su QP, Wu MCL, Liu Y, Wang B, Li D, Shan X, Kianinia M, Aharonovich I, Toth M, Jackson SP, Xi P, Jin D. *Nat Commun*, 2018, 9: 3290
- 110 Dong H, Sun LD, Feng W, Gu Y, Li F, Yan CH. *ACS Nano*, 2017, 11: 3289–3297
- 111 Huang B, Wu Q, Peng X, Yao L, Peng D, Zhan Q. *Nanoscale*, 2018, 10: 21025–21030
- 112 Gu Y, Guo Z, Yuan W, Kong M, Liu Y, Liu Y, Gao Y, Feng W, Wang F, Zhou J, Jin D, Li F. *Nat Photonics*, 2019, 13: 525–531
- 113 Chen H, Jiang Z, Hu H, Kang B, Zhang B, Mi X, Guo L, Zhang C, Li J, Lu J, Yan L, Fu Z, Zhang Z, Zheng H, Xu H. *Nat Photon*, 2022, 16: 651–657
- 114 Ou X, Qin X, Huang B, Zan J, Wu Q, Hong Z, Xie L, Bian H, Yi Z, Chen X, Wu Y, Song X, Li J, Chen Q, Yang H, Liu X. *Nature*, 2021, 590: 410–415
- 115 Pei P, Chen Y, Sun C, Fan Y, Yang Y, Liu X, Lu L, Zhao M, Zhang H, Zhao D, Liu X, Zhang F. *Nat Nanotechnol*, 2021, 16: 1011–1018
- 116 Abbe E. *Archiv für Mikroskopische Anatomie*, 1873, 9: 413–468
- 117 Peng X, Huang B, Pu R, Liu H, Zhang T, Widengren J, Zhan Q, Ågren H. *Nanoscale*, 2019, 11: 1563–1569
- 118 Mi Z, Zhang Y, Vanga SK, Chen CB, Tan HQ, Watt F, Liu X, Bettiol AA. *Nat Commun*, 2015, 6: 8832
- 119 Wen S, Liu Y, Wang F, Lin G, Zhou J, Shi B, Suh YD, Jin D. *Nat Commun*, 2020, 11: 6047
- 120 Wu R, Zhan Q, Liu H, Wen X, Wang B, He S. *Opt Express*, 2015, 23: 32401
- 121 Zhang H, Jia T, Chen L, Zhang Y, Zhang S, Feng D, Sun Z, Qiu J. *Phys Chem Chem Phys*, 2017, 19: 17756–17764
- 122 Kolesov R, Reuter R, Xia K, Stöhr R, Zappe A, Wrachtrup J. *Phys Rev B*, 2011, 84: 153413
- 123 Klar TA, Jakobs S, Dyba M, Egner A, Hell SW. *Proc Natl Acad Sci USA*, 2000, 97: 8206–8210
- 124 Chen C, Liu B, Liu Y, Liao J, Shan X, Wang F, Jin D. *Adv Mater*, 2021, 33: 2008847
- 125 Wu Q, Huang B, Peng X, He S, Zhan Q. *Opt Express*, 2017, 25: 30885
- 126 Liu Y, Wang F, Lu H, Fang G, Wen S, Chen C, Shan X, Xu X, Zhang L, Stenzel M, Jin D. *Small*, 2020, 16: 1905572
- 127 Göppert-Mayer M. *Ann Phys*, 1931, 401: 273–294
- 128 Su Q, Han S, Xie X, Zhu H, Chen H, Chen CK, Liu RS, Chen X, Wang F, Liu X. *J Am Chem Soc*, 2012, 134: 20849–20857
- 129 Rabouw FT, Prins PT, Villanueva-Delgado P, Castelijns M, Geitenbeek RG, Meijerink A. *ACS Nano*, 2018, 12: 4812–4823
- 130 Liu X, Wang Y, Li X, Yi Z, Deng R, Liang L, Xie X, Loong DTB, Song S, Fan D, All AH, Zhang H, Huang L, Liu X. *Nat Commun*, 2017, 8: 899
- 131 Zheng W, Zhou S, Chen Z, Hu P, Liu Y, Tu D, Zhu H, Li R, Huang M, Chen X. *Angew Chem*, 2013, 125: 6803–6808
- 132 Zheng W, Tu D, Huang P, Zhou S, Chen Z, Chen X. *Chem Commun*, 2015, 51: 4129–4143
- 133 Kong M, Gu Y, Liu Y, Shi Y, Wu N, Feng W, Li F. *Small*, 2019, 15: 1904487
- 134 Zhao M, Li B, Wu Y, He H, Zhu X, Zhang H, Dou C, Feng L, Fan Y, Zhang F. *Adv Mater*, 2020, 32: 2001172
- 135 Zhao M, Zhuang H, Zhang H, Li B, Ming J, Chen X, Chen M. *Angew Chem Int Ed*, 2022, 61: e202209592
- 136 Fikouras AH, Schubert M, Karl M, Kumar JD, Powis SJ, Di Falco A, Gather MC. *Nat Commun*, 2018, 9: 4817
- 137 Jin L, Wu Y, Wang Y, Liu S, Zhang Y, Li Z, Chen X, Zhang W, Xiao S, Song Q. *Adv Mater*, 2019, 31: 1807079
- 138 Shang Y, Zhou J, Cai Y, Wang F, Fernandez-Bravo A, Yang C, Jiang L, Jin D. *Nat Commun*, 2020, 11: 6156
- 139 Zhu H, Chen X, Jin LM, Wang QJ, Wang F, Yu SF. *ACS Nano*, 2013, 7: 11420–11426
- 140 Wu Y, Xu J, Poh ET, Liang L, Liu H, Yang JKW, Qiu CW, Vallée RAL, Liu X. *Nat Nanotechnol*, 2019, 14: 1110–1115
- 141 Qin X, Carneiro Neto AN, Longo RL, Wu Y, Malta OL, Liu X. *J Phys Chem Lett*, 2021, 12: 1520–1541
- 142 Wu M, Ha ST, Shendre S, Durmusoglu EG, Koh WK, Abujetas DR, Sánchez-Gil JA, Paniagua-Domínguez R, Demir HV, Kuznetsov AI. *Nano Lett*, 2020, 20: 6005–6011
- 143 Fernandez-Bravo A, Wang D, Barnard ES, Teitelboim A, Tajon C, Guan J, Schatz GC, Cohen BE, Chan EM, Schuck PJ, Odom TW. *Nat Mater*, 2019, 18: 1172–1176
- 144 Shang Y, Chen T, Ma T, Hao S, Lv W, Jia D, Yang C. *J Rare Earths*, 2022, 40: 687–695
- 145 Wang T, Yu H, Siu CK, Qiu J, Xu X, Yu SF. *ACS Photonics*, 2017, 4: 1539–1543
- 146 Fernandez-Bravo A, Yao K, Barnard ES, Borys NJ, Levy ES, Tian B, Tajon CA, Moretti L, Altoe MV, Aloni S, Beketayev K, Scotognella F, Cohen BE, Chan EM, Schuck PJ. *Nat Nanotech*, 2018, 13: 572–577
- 147 Chang SW, Lin TR, Chuang SL. *Opt Express*, 2010, 18: 15039–15053
- 148 Austerlitz H. Chapter 2—*Analog signal transducers in Data Acquisition Techniques Using PCs*. 2nd Ed. San Diego: Academic Press, 2003. 6–28
- 149 le Masne de Chermont Q, Chanéac C, Seguin J, Pellé F, Maîtrejean S, Jolivet JP, Gourier D, Bessodes M, Scherman D. *Proc Natl Acad Sci USA*, 2007, 104: 9266–9271
- 150 Wang JX, Bakr OM, Mohammed OF. *Matter*, 2022, 5: 2547–2549
- 151 Qin X, Liu X, Huang W, Bettinelli M, Liu X. *Chem Rev*, 2017, 117: 4488–4527
- 152 Yang YM, Li ZY, Zhang JY, Lu Y, Guo SQ, Zhao Q, Wang X, Yong ZJ, Li H, Ma JP, Kuroiwa Y, Moriyoshi C, Hu LL, Zhang LY, Zheng LR, Sun HT. *Light Sci Appl*, 2018, 7: 88
- 153 Bian H, Qin X, Wu Y, Yi Z, Liu S, Wang Y, Brites CDS, Carlos LD, Liu X. *Adv Mater*, 2022, 34: 2101895
- 154 Li Y, Gecevicius M, Qiu J. *Chem Soc Rev*, 2016, 45: 2090–2136
- 155 Li L, Li T, Hu Y, Cai C, Li Y, Zhang X, Liang B, Yang Y, Qiu J. *Light Sci Appl*, 2022, 11: 51
- 156 Takasaki H, Tanabe S, Hanada T. *J Ceram Soc Jpn*, 1996, 104: 322–326

- 157 Lei L, Wang Y, Xu W, Ye R, Hua Y, Deng D, Chen L, Prasad PN, Xu S. *Nat Commun*, 2022, 13: 5739
- 158 Evans KA, Kennedy ZC, Arey BW, Christ JF, Schaefer HT, Nune SK, Erikson RL. *ACS Appl Mater Interfaces*, 2018, 10: 15112–15121
- 159 Elder B, Neupane R, Tokita E, Ghosh U, Hales S, Kong YL. *Adv Mater*, 2020, 32: 1907142
- 160 Huang J, Wu P. *Nano-Micro Lett*, 2021, 13: 15
- 161 Ni R, Qian B, Liu C, Liu X, Qiu J. *Opt Express*, 2018, 26: 25481–25491
- 162 Liu J, Guo Y, Bi Y, Wang Y, Wang Y, Kipper MJ, Belfiore LA, Tang J. *J Alloys Compd*, 2022, 928: 167194
- 163 Yao Y, Yin C, Hong S, Chen H, Shi Q, Wang J, Lu X, Zhou N. *Chem Mater*, 2020, 32: 8868–8876
- 164 Méndez-Ramos J, Ruiz-Morales JC, Acosta-Mora P, Khaidukov NM. *J Mater Chem C*, 2016, 4: 801–806
- 165 Rocheva VV, Koroleva AV, Savelyev AG, Khaydukov KV, Generalova AN, Nechaev AV, Guller AE, Semchishen VA, Chichkov BN, Khaydukov EV. *Sci Rep*, 2018, 8: 3663
- 166 Chen Y, Zhang J, Liu X, Wang S, Tao J, Huang Y, Wu W, Li Y, Zhou K, Wei X, Chen S, Li X, Xu X, Cardon L, Qian Z, Gou M. *Sci Adv*, 2020, 6: eaba7406
- 167 Hososhima S, Yuasa H, Ishizuka T, Hoque MR, Yamashita T, Yamanaka A, Sugano E, Tomita H, Yawo H. *Sci Rep*, 2015, 5: 16533
- 168 Wu X, Zhang Y, Takle K, Bilsel O, Li Z, Lee H, Zhang Z, Li D, Fan W, Duan C, Chan EM, Lois C, Xiang Y, Han G. *ACS Nano*, 2016, 10: 1060–1066
- 169 Lin X, Wang Y, Chen X, Yang R, Wang Z, Feng J, Wang H, Lai KWC, He J, Wang F, Shi P. *Adv Healthcare Mater*, 2017, 6: 1700446
- 170 Chen S, Weitemier AZ, Zeng X, He L, Wang X, Tao Y, Huang AJY, Hashimoto Y, Kano M, Iwasaki H, Parajuli LK, Okabe S, Teh DBL, All AH, Tsutsui-Kimura I, Tanaka KF, Liu X, McHugh TJ. *Science*, 2018, 359: 679–684
- 171 Liang L, Chen J, Shao K, Qin X, Pan Z, Liu X. *Nat Mater*, 2023, 22: 289–304
- 172 Hou B, Yi L, Li C, Zhao H, Zhang R, Zhou B, Liu X. *Nat Electron*, 2022, 5: 682–693